Impact of the cancer endocycle on cell survival after therapy

Chi-Ju Kim[1,†], Anna LK Gonye[1,2,†], Kevin Truskowski[1,2], Cheng-Fan Lee[1], Yoon-Kyoung Cho[3,4], Kenneth J Pienta[1,2], Robert H. Austin[5], Sarah R Amend[1,2]

1. Cancer Ecology Center, The Brady Urological Institute, Johns Hopkins School of Medicine, 600 N. Wolfe St., Baltimore, MD, 21287, USA.
2. Cellular and Molecular Medicine Graduate Program, Johns Hopkins School of Medicine, 600 N. Wolfe St., Baltimore, MD, 21287, USA.
3. Department of Biomedical Engineering, Ulsan National Institute of Science and Technology (UNIST), Ulsan 44919, Republic of Korea
4. Center for Soft and Living Matter, Institute for Basic Science (IBS), Ulsan 44919, Republic of Korea
5. Department of Physics, Princeton University, Princeton, New Jersey 08544, USA.

†. Contributed equally.

*Robert H. Austin, Chi-Ju Kim; Sarah R Amend.

Email: austin@princeton.edu, ckim143@jhmi.edu; samend2@jhmi.edu

Author Contributions: Kim, C-J: conceptualization, methodology, investigation, writing (original draft), writing (review and editing), visualization. Gonye, ALK: conceptualization, methodology, investigation, writing (original draft), writing (review and editing), visualization. Truskowski, K: methodology, investigation. Lee, C-F: investigation. Cho, Y-K: conceptualization, writing (review and editing), funding acquisition. Austin, RH: conceptualization, writing (review). Pienta, KJ: conceptualization, writing (review and editing), funding acquisition. Amend, SR: conceptualization, writing (review and editing), funding acquisition.

Competing Interest Statement: K.J.P. is a consultant for CUE Biopharma, Inc., and holds equity interest in CUE Biopharma, Inc., Keystone Biopharma, Inc. and PEEL Therapeutics, Inc. S.R.A. holds equity interest in Keystone Biopharma, Inc.

Classification: Biological Sciences, Cell Biology.

Keywords: cancer therapy resistance, polyaneuploid cancer cell (PACC) state, nuclear morphology, polyploidy

This PDF file includes:
Main Text
Figures 1 to 6

Abstract

We characterized nuclear morphology and function as cancer cells underwent chemotherapeutic treatment and recovery to identify the unique characteristics that are associated with treatment resistance and successful survival. We found that one way cancer cells can survive systemic therapy is to enter the polyaneuploid cancer cell (PACC) state, a recently-described mechanism of therapy resistance. Cancer cells in this state are physically enlarged, undergo whole-genome doubling resulting in polyaneuploid genomes, and are associated with worse prognosis in cancer patients. The PACC state is accessed when a cancer cell experiences external stress, such as genotoxic chemotherapy; after a period of recovery, cells exit the PACC state and resume

proliferation to repopulate the tumor cell pool. We discovered that cells that survive after therapy are predominantly mononucleated and have increasing nuclear size, enabled by continuous endocycling. We further found that cells in the PACC state are likely to employ more efficient DNA damage repair. Lastly, while many cancer cells treated with a genotoxic agent succumb to apoptosis shortly after treatment, our data suggest that surviving cancer cells must strike a balance of autophagy to restore cellular homeostasis while avoiding autophagic cell death. Overall, our findings demonstrate the fate of cancer cells following chemotherapy treatment and define key characteristics of the resistant PACC state that is accessed via endocycling. This work is essential for understanding and, ultimately, targeting, cancer resistance and recurrence.

Significance Statement

Accession of the PACC state has recently been appreciated as a mechanism for therapy resistance and recurrence in cancer. We found that cancer cells following treatment undergo endocycling, a non-mitotic cell cycle variant, resulting in increased cell and nuclear size. The PACC state is often defined as a multinucleated and/or multilobular. Here, for the first time, we show that uniformly mononucleated PACCs not only exist, but become the majority cell type during cellular recovery after therapy, making them a prime suspect for seeding a therapeutically resistant recurrence. Overall, our findings imply that mononucleated cells in the PACC state continue to replicate DNA by endocycling and repair DNA damage, but multinucleated cells that initially survive therapy eventually undergo autophagic cell death.

Main Text

Introduction

Once cancer has metastasized, it is incurable because tumors evolve resistance to virtually all systemically administered anticancer therapies. Classically, this has been attributed to the presence of cancer stem cells or genetically heterogeneous subsets of cancer cells within the tumor, which allow for continued survival of a cancer cell population due to the presence of a resistant clone or clones (1-22). However, our group and others have identified a stress-induced cell state characterized by physical enlargement and polyaneuploid genomes. Cells in the polyaneuploid cancer cell (PACC) state have been identified in the tumors of patients with metastatic prostate cancer (PCa) and in other tumor types (23-33). Presence of cells in the PACC state in clinical radical prostatectomy specimens from PCa patients is predictive of an increased risk of disease progression (34). The PACC state is initiated when a cancer cell is subjected to a stressor, such as chemotherapy or radiotherapy, triggering a conserved evolutionary program that results in sustained polyploidization of the aneuploid genome (polyaneuploidy) and increased cell size and cell contents. When the cellular stressor is no longer present and after a period of recovery, a subpopulation of cells may exit the PACC state and reinitiate proliferation, a phenomenon clinically observed as cancer recurrence (23-33, 35-42).

The PACC state is the result of a noncanonical cell cycle that bypasses cell division in response to environmental stress (25, 43-47). Skipping mitosis and/or cytokinesis results in the increase of cellular contents, including nuclear size and genomic material, and is hypothesized to aid the cell in adapting to toxic environments such as therapeutic stress (23, 26, 28, 31, 32). Additionally, the increased genomic content may help prevent cells in the PACC state from undergoing cell cycle checkpoint-activated apoptosis due to DNA damage (23-33, 35-42, 48). The amitotic cell cycle that creates the genomic duplication characteristic of the PACC state can be characterized as mitotic slippage, endocycling, or endomitosis (49-52), and is accompanied by abnormal nuclear morphologies including large mononucleated, mononucleated and simultaneously lobulated, or

multinucleated phenotypes (26-32, 42). It is likely that the specific nuclear morphology of PACCs plays a role in the survival and eventual formation of progeny by these cells.

Abnormal nuclear morphology is often conspicuous in cancer cells (53-63). Such phenotypes may arise from the intrinsic physiological properties of cancer cells (i.e., the dysregulation of the cell cycle) and cause aneuploidy, genomic instability, and abnormal gene and protein expression patterns including genomic alterations of nuclear envelope-associated proteins (63). It has been shown that irregular and large nuclear shapes reflect malignancy (54, 56, 61-63). Historically, increased variation in nuclear size and shape has been regarded as a significant pathologic parameter and used clinically for the diagnosis of various cancers (63, 64). Hyper-abnormal nuclear morphologies, such as multilobulated and multinucleated nuclei, are highly associated with metastasis and recurrence (35, 54, 65). Since cancer cells in the PACC state exhibit most or all of these distinct nuclear shapes associated with malignancy (54, 56, 61-63) and because recent evidence suggest that the PACC state could be the lynchpin of cancer lethality (23-33, 35-42), it is important to investigate the timing and mechanisms utilized by cancer cells to enter and maintain the therapeutic resistant PACC state.

To study the biology of the PACC state, in particular the life history of cells following chemotherapy treatment that successfully access the PACC state versus those that die after chemotherapy, we characterized nuclear morphology and function over time following treatment release. For the first time, we demonstrate that mononucleated polyploid cells dominate the population that survive the weeks following therapy and thus represent a strong candidate to eventually seed therapeutic resistant population. These data indicate that cells that survive cisplatin treatment access a mononucleated PACC state continue to replicate DNA via endocycling and retain high levels of DNA damage repair, while multinucleated cells that initially survive therapy eventually undergo autophagic cell death.

Results

Classification of nucleus morphology in cancer cells following treatment release

Cancer cell lines were treated with [LD50] concentrations of cisplatin for 72 hours, media was replaced, and cultures were allowed to recover for various time periods. We observed the expected cell die off at 72 hours, and all following studies were performed on the surviving cell populations at each time point. First, we classified the morphology of treated cancer cell nuclei as mononucleated or multinucleated. Treated cancer cell nuclear morphology was visualized by immunofluorescent 2D (**Fig. 1A**) and 3D (**Fig. 1B**) imaging in. Conventional nuclear visualization in 2D by DNA staining with DAPI or Hoechst alone is not always suitable for distinguishing between types of nucleus morphology (**Fig. S1**). The nuclear envelope (NE) of cells was visualized by performing immunofluorescent labeling of lamin A/C, an abundant structural component of the NE to enhance visualization to discriminate nuclear morphology (**Fig. 1A**). Immediately after removal from cisplatin treatment, treated PC3 cells exhibited a uniformly distributed nuclear morphology, with the proportion of mono- and multinucleates each approximately 50% (**Fig. 1A, C**). As PC3 cells recovered, the population ratio shifted, with mononucleates becoming predominant over the course of recovery (**Fig. 1C**), conversely indicating that multinucleated treated cells are not viable and eventually die. Our 2D methodology underestimated the number of multinucleates at the early time points due to a spatially hindering effect of the nuclear envelope signal (**Fig. S2**). We confirmed this finding by 3D confocal microscopy imaging of treated cells (**Fig. 1B, D**). Live cells were embedded in Matrigel to maintain cellular structure, their nuclei and cytoplasm were fluorescently visualized, and 3D nuclear structures were rendered. The shift to a majority mononucleate

morphology in the recovered PC3 population recapitulated what was observed in the 2D analysis (**Fig. 1D**).

Characterization of nuclear and cell size following treatment release

We characterized how treated cell volume and nuclear volume changed over time by assessing cytoplasmic and nuclear volumes measured by 3D confocal microscopy. The nuclear volumes of surviving cells continuously increased as a function of recovery time (**Fig. 2A**). Nuclear volume increased in correlation with increased cell volume (**Fig. 2A, B**). To determine the extent to which the nuclear size was influenced by cytoskeletal/cytoplasmic components, we measured the area of isolated nuclei. The nuclear envelope of the isolated nuclei was fluorescently labeled with an anti-lamin A/C antibody and visualized with immunofluorescence microscopy (**Fig. 2C, D**). Consistent with the whole-cell data, the size of isolated nuclei increased as a function of the recovery time (**Fig. 2D**).

Cancer cell endocycling increases nuclear size

The increasing nuclear size of the surviving cells suggested that mononucleated cells undergo repeated DNA duplication during the recovery period following cisplatin treatment. We utilized a fluorescence ubiquitination cell cycle indicator (FUCCI) cell cycle sensor assay (see FUCCI construct (66), **Fig. S3**). The nuclei of cells transduced with the FUCCI construct fluoresce red in G1, yellow (double positive for red and green) in very early S, green in mid-late S, G2, and up to anaphase in M, and are colorless in late-M and G0. Using live cell imaging, we observed large cisplatin-treated cells progressing through these different stages without undergoing cell division, indicating that the cells underwent endocycling (**Fig. 2E**). To specifically test DNA replication, cultures were pulsed with thymidine analogue EdU for 20 hours and EdU incorporation was visualized with immunofluorescence imaging (**Fig. 2E, F**). Positive staining showed that mononucleated cells were actively engaged in *de novo* DNA synthesis at all timepoints following removal of cisplatin (**Fig. 2F**). These findings indicate that surviving cells, while not proliferative, are functionally active in genome duplication, although certain cellular behaviors (i.e., lack of division) suggest a temporary functional dormancy.

We further investigated the qualitative 3D morphological features of post-treatment PC3 nuclei. The nucleus-to-cytoplasm ratio (NC ratio) gradually decreased as a function of recovery time (**Fig. 2G**). This implies that the rate of synthesis of non-nuclear biomolecules is relatively faster than genomic replication compared to treatment-naive cells. We also observed that the sphericity of nuclei gradually decreased over recovery (**Fig. 2H, Fig. S4**), suggesting that nuclei at later time points may exhibit low rigidity or high deformability, perhaps due to a lower supporting force derived from their cytoskeleton (54, 61, 67-70).

Nucleolar size and number following cisplatin treatment release

The nucleolus, the largest substructure of the nucleus, is a ribosomal RNA production hub and plays a significant role in nuclear homeostasis (71-74). It has been reported that the size and number of nucleoli are highly correlated with enhanced cell proliferation and malignancy in cancers (71-77). We investigated differences in nucleolar structure between non-treated cancer cells and cancer cells at different timepoints following cisplatin therapy (**Fig. 3**). The number of nucleoli within the nuclei of treated PC3 cells decreased (**Fig. 3A, B**), while the average size of each nucleolus increased (**Fig. 3A, C**) as a function of recovery time. The nucleolus to the nucleus area ratio in treated cells initially decreased at early time points (until day 3) and rebounded during recovery (**Fig. 3D**). These results indicate that the synthesis of nucleolar molecules was slower than that of nuclear molecules in treated cells; however, nucleolar size returns to relative levels similar to untreated controls, suggesting the potential of nucleoli to actively respond to genomic stress during treatment recovery to maintain nuclear homeostasis (73, 74, 76-78) (**Fig. 3C**).

In its function as a ribosomal RNA production hub, a nucleolus contains genes for rRNAs (5.8S, 18S, and 28S rRNAs) that are transcribed as a single unit within the nucleolus (71-74). RNA gel electrophoresis showed that the level of 28S rRNA in treated PC3 cells was higher than that in

parental cells and increased as a function of recovery time. 18S rRNA expression was lower in treated cells and the level of 5.8S rRNA remained similar in intensity in the treated cells until 10 days after therapy release (**Fig. S5**). The altered rRNA composition of cells recovering from cisplatin treatment suggests that the remodeling of rRNA configuration in the nucleolus may be a response to genomic stress.

Quantification of DNA damage responses in the PACC state

Following release of cisplatin treatment, the death rate gradually decreased as a function of recovery time and reached a plateau (**Fig. 4A-B**). The DNA damage response (DDR) plays a crucial role in avoiding programmed cell death and prolonging cellular life (79, 80). gH2AX foci mark DNA damage loci, and 53BP1 molecules are recruited to DNA damage to initiate the DNA repair pathway, forming distinct foci at sites damaged DNA loci (79, 80). Defective recruitment of 53BP1 to damaged DNA can result in DDR failure, eventually inducing cell death (79, 81-83). Expression and colocalization of gH2AX and 53BP1 foci was assessed for each recovery time point (**Fig. 4C, D**). Early in recovery (days 1 and 3), treated PC3 cells had a low level of colocalization, but the colocalized gH2AX/53BP1 foci returned to the level of the untreated cancer cell control at day 10 post-treatment. Furthermore, we found that the size of gH2AX foci decreased, whereas the size of 53BP1 foci increased following therapy from day 1 to day 10 (**Fig. S6**). These findings suggest that surviving cells activate the DDR pathway to avoid cell death (84, 85).

The absolute counts of gH2AX and 53BP1 foci per unit nuclei area were also calculated (**Fig. 4E, F**). Excessive DNA damage induces acute apoptosis and exhibits a distinct gH2AX pan-staining pattern (86-88). Pan-stained nuclei were evaluated independently and excluded from the foci counts to avoid artifacts of extreme foci counts. The proportion of gH2AX pan-stained nuclei in treated cells was approximately half of the total population at day 1 and 30% at day 3, gradually decreasing during the remaining of the recovery points examined (**Fig. S7A**). The exclusion of many pan-stained nuclei in the early recovered population led to a highly underscored absolute value of gH2AX foci, especially day 1 and day 3, which is not represented in the colocalization ratio (**Fig. 4D**). Nuclei with 53BP1 pan-staining were not observed; thus, the absolute value of 53BP1 foci counts per area itself indicates that they decreased until day 3 and increased to pre-treatment levels by the later treatment recovery timepoints (**Fig. 4F**).

Mononucleate cells became the dominant population over the duration of treated cell recovery (**Fig. 1C**), suggesting that multinucleated cancer cells died. To investigate the relevance of these two nuclear morphologies in the function of the DDR, the level of colocalization between gH2AX and 53BP1 foci in each types was compared (**Fig. 4G**). Mononucleate cells contain more colocalized DDR foci than multinucleates, indicating that the maintenance of single, large nucleus is a key feature of the resilient surviving cancer cells.

The mechanism of death in cells following treatment release

The level of apoptosis in treated cells was initially assessed by annexin-V assay by flow cytometry analysis. As expected, the annexin-V staining was higher in the treated cells compared to parental but decreased with increased recovery time out to three days post-treatment (**Fig. 5A**). These data indicate that the relative level of apoptotic cell death decreases during recovery and suggest that apoptosis is unlikely to be the predominant cell death mechanism in cells that initially survive the cisplatin therapy.

Autophagy is regarded as a cell survival program that helps to maintain cellular homeostasis (89-94). Evidence in the literature suggests that autophagy can also play a role in cell death. Broadly, autophagic cell death is a type of cell death that is accompanied by high amounts of autophagic vacuolization of the cytoplasm, often in the absence of complete chromatin condensation (95). We labeled autophagosomes and autolysosomes and evaluated staining by flow cytometry. We found that treated cancer cells had increased levels of autophagy compared to treatment-naïve controls, and this level increased with time post-treatment removal (**Fig. 5B**). We further investigated the level of autophagy at later recovery time points (days 5 and 10) by visualizing autophagosomes

and/or autolysosomes via immunofluorescence microscopy (**Fig. 5C**). The volumetric quantification of autophagic vesicles inside cells (**Fig. 5D, E**) demonstrated that the level of autophagy rapidly increased immediately after treatment and gradually increased during recovery (**Fig. 5F**). Since the cellular volume of treated cells continuously increased (**Fig. 2B**), the number of autophagosomes was normalized to cellular volume. The number of autophagosomes per unit volume increased until day 3 of the recovery period and remained elevated through day 10 (**Fig. 5G**). Interestingly, the size of autophagosomes also increased as a function of recovery time (**Fig. 5H**). Increased expression of autophagy markers (LC3B-I and LC3b-II) by western blot (**Fig. 5I, J**). These data indicate that the level of autophagy in surviving cells post-treatment is significantly higher than that of the parental cell population.

As cells at early time points in recovery have been reported to contain micronuclei and fragmented cytoplasmic DNA (96-99), we hypothesized that nucleophagy, or the autophagy of genomic contents, may contribute to the observed increased levels of autophagy over recovery time. We fluorescently labeled autophagosomes by staining for LC3B, a representative autophagy marker, while simultaneously probing for gH2AX, lamin A/C, and DAPI (**Fig. 5K**). Cells undergoing nucleophagy were readily observed in the treated population 3 days post-treatment, suggesting that excessive nucleophagy early in recovery may contribute to autophagic cell death. Of note, the portion of multinucleated cells dramatically decreases after day 5 of the recovery period, converse to the pattern of increasing autophagosome counts per volume.

Consideration of the cell-line heterogeneity and drug-type dependency

To identify cell type- and drug-specific phenotypic responses to treatment and recovery, we assessed breast cancer cell line MDA-MB-231 and treatment with common chemotherapies docetaxel (microtubule stabilizer) and etoposide (topoisomerase II inhibitor).

MDA-MB-231 cells exhibited a different pattern of nuclear morphology than PC3 cells after treatment with [LD50] cisplatin. The proportion of multinucleated cells increased during recovery (**Fig. S8**). Upon investigation of the DDR in treated MDA-MB-231s, we observed that the colocalization ratio of gH2AX and 53BP1 was initially high at day 1 but decreased until day 5 before returning to an elevated level in the recovered population by days 10 and 15 post-therapy removal (**Fig. S9**). The ratio of gH2AX pan-stained nuclei was lower in treated MDA-MB-231 cells than in PC3 cells at day 1 of the recovery period (**Fig. S7**). Both gH2AX and 53BP1 counts per area gradually decreased during recovery (**Fig. S9**). Notably, most parental MDA-MB-231 cells do not express both gH2AX and 53BP1 foci. It was also confirmed that the level of DDR in mononucleated cells was higher than that in multinucleated cells (**Fig. S9, Fig. S10**). Taken together, the initially active DDR in treated MDA-MB-231 cells may result in the delay in the formation of multinucleate cells in this cell line model. Consequently, the relative number of surviving MDA-MB-231 cells at each recovery time point was higher than observed in PC3 (**Fig. S11A**), so the death rate was lower at early time points of the recovery period (**Fig. S11B**).

A primary mechanism of multinucleate formation is a mitotic catastrophe (26, 27, 31, 100-105). The proportion of nuclei that underwent a mitotic catastrophe in both PC3 and MDA-MB-231 was determined by examining immunofluorescently labeled images of the nuclear envelope (**Fig. S12**). The results indicate that multinucleated treated MDA-MB-231 cells have a lower proportion of cells with mitotically catastrophic nuclei compared to treated PC3 cells at early time points in the recovery period, but proportions increased as recovery time increased. These findings suggest that an active DDR suppresses multinucleation due to mitotic catastrophe, preventing cell death.

To evaluate the effect of different treatments on multi- vs mononucleation in treated cells, PC3 cells were treated with [LD50] doses of chemotherapeutic drugs etoposide and docetaxel for 72 hours (**Fig. S13**). The proportion of multinucleates was significantly different between the two drugs and compared to cisplatin. The trend of increased mononucleate morphology at later recovery times was consistent with cisplatin treatment. Differences in the multinucleation level in the docetaxel treatment group are likely due to the mechanism of this therapy, which stabilizes microtubules to

inhibit cell proliferation (106). These results suggest that mononucleated PC3 cells will eventually become a dominant morphological phenotype in the longer recovery period.

Discussion

In this study, we explored the life history of cells following chemotherapy treatment that survive and successfully undergo polyploidization and access the PACC state versus those that die in the days and weeks after chemotherapy. Our data indicate that there are multiple exclusive trajectories of cancer cells subjected to genotoxic stress, including both cell death after therapy release and accession of the PACC state (**Fig. 6**). We found that cells that resist initial death due to therapy undergo multiple rounds of genome duplication without cell division in a process of endocycling, and have a more active DDR. They increase levels of autophagy, which may lead to nucleophagy or autophagic cell death, but paradoxically may represent resiliency against therapeutic stress. Cells that enter the PACC state exist in a functionally dormant state that can be described distinct observed phenotypes: 1) non-proliferative, 2) active and continued genomic duplication via endocycling, 3) active nucleoli, and 4) continued DDR. These findings represent a new understanding of the way cancer cells resist cytotoxic therapy and contribute to cancer lethality.

It has recently been appreciated that cancer cells in the PACC state are important players in tumor biology, specifically related to therapy resistance and cancer recurrence. We have shown that cancer cells access the PACC state via a polyploidization program in response to genotoxic chemotherapies. The resulting enlargement of both nuclear and cell size is hypothesized to aid the cell in adapting to toxic environments such as therapeutic stress. Prior to this study, it was widely regarded that one key feature of cells in the PACC state is their multinucleated and/or multi-lobulated nuclei (35-37, 107-110). Through 2D and 3D immunofluorescence microscopy, we demonstrated that not only do mononucleated PACCs exist, but that mononucleates become the predominant cell type over the course of cellular recovery from cisplatin, docetaxel, and etoposide therapy.

We found that the cells in the PACC state engage in active DNA replication without entry into mitosis endocycling, providing a mechanistic explanation for the increase in nuclear size that we observed in this study and that others have observed in studies of similar large, polyploid cancer cells (26, 35-37, 109-112). Cells in the PACC state are not simply cancer cells that are stalled at the G2/M DNA damage checkpoint in mitosis; rather, they bypass this checkpoint completely. Interestingly, while the percentage of cells that actively incorporating EdU decreased as a function of recovery time, indicating that the endocycling program accessed by the cells might be more important or relevant earlier in treatment recovery, cytoplasmic volumes steadily increased in a manner that suggests consistent biosynthesis of contents beyond genomic material.

The nucleolus plays a crucial role in nuclear homeostasis as an RNA production hub (71-74). Both the size and number of nucleoli are highly correlated with cancer malignancy and have previously been used as a diagnostic signature (77). Cells in the PACC state showed a distinct nucleolar phenotype, with fewer nucleoli of a larger size (**Fig. 4B, D**). This distinct pattern may be a consequence of endocycling, wherein the mitotic phase is completely bypassed, since the nucleolar structure disassembles at the mitotic phase and reassembles at interphase (71). To our knowledge, a distinct pattern of nucleolar size and number has not been reported in the cancer biology field, but it has been shown that stem cells often have fewer but larger nucleoli than differentiated somatic cells (113). Other studies of large, polyploid cancer cells have suggested that these cells may act as a type of cancer stem cell, possessing stem cell-like features and cellular programs (23, 26, 31-33, 35, 37). Together, our results suggest two functional consequences for PACC biology: mononucleated cells in the PACC state may be functionally dormant (i.e., nondividing yet active), and they may have a higher potential to differentiate into therapeutic-resistant progeny with a level of phenotypic plasticity due to similarities to stem cells.

A final focus of this paper was to characterize the extent to which DNA damage and the cellular response to this damage impact both the shift in nuclear morphology of treated cells, both those that eventually die and those that access the pro-survival PACC state. We observed that immediately after treatment, cells display a high level of DNA damage, measured via staining of gH2AX. This was visible both as gH2AX foci representing sites of DDR machinery recruitment, as well as pan-stained nuclei, representing excessive and widespread DNA damage that induces acute apoptosis (16, 87, 88). Treated cells initially had a high rate of pan-stained gH2AX (~50%) that decreased as cells recovered (**Fig. S5**). This suggests that treated cells with pan-stained nuclei are non-viable and destined for death early following therapy release, while cells with gH2AX foci are more likely have successful DDR and access the PACC state.

While gH2AX indicates DNA damage, it is not sufficient to assess the level of repair. 53BP1 localizes to sites of DNA damage and recruits the downstream effectors of DNA repair via the Non-Homologous End Joining (NHEJ) pathway such as RIF1 and PTIP (82, 114-116). 53BP1 nuclear pan-staining, recognized as a failure of its recruitment to DNA damage sites (82, 88, 117-119), was not observed. 53BP1 foci count (**Fig. 5F**) indicated that DNA repair protein recruitment was decreased at early time points of the recovery and later returned to a similar level of untreated cells. To capture the level of DDR, indicated by the recruitment of DNA repair molecules to sites of DNA damage, we assessed colocalization of gH2AX and 53BP1 that indicated that the DDR increased over recovery time. Simultaneously, the relative death rate of treated cells decreased over time (**Fig. 5B**). It is worthwhile to note that canonical Homologous Recombination (HR) pathway is active at S/G2 phase, whereas NHEJ pathway plays a role in acute repair of DNA damage at all phases of the cell cycle (82, 88, 120-124). The DDR foci analysis (**Fig. 5D-G**) suggest that the NHEJ pathway is a primary mechanism of the DDR in the PACC state.

We observed that the level of apoptosis decreased in populations of treated cells over time in a pattern similar to the decrease in gH2AX pan-stained nuclei. Conversely, autophagy increased throughout cell recovery, suggesting that cells in the PACC state require a higher level of autophagy to maintain cellular homeostasis. It is also likely that that for some treated cells, the high level of autophagy, more specifically nucleophagy, may play a role in cell death at later timepoints through the induction of autophagic cell death (95). Together, our interrogation of DNA damage, apoptosis, and cell death present a paradigm where soon after therapy release, the population contains a higher proportion of cells with a high level of widespread DNA damage that induces apoptosis, while with recovery time, there is a shift towards a lower relative rate of cell death with some cells dying due to an overwhelming amount of autophagy secondary to DNA damage that was never resolved.

Both nuclei and cytoplasm volume were found to be higher in treated cells than treatment-naïve controls. The NC ratio has been regarded as a morphologic feature for the diagnosis of tumor malignancy: a higher NC ratio indicates high malignancy (61, 63, 125), while a low NC ratio is associated with the phenotypes of cell cycle arrest, replicative aging, senescence exhibiting lower cell function and proliferative potential, and lower RNA and protein concentrations (126). Interestingly, while PC3 cells in the PACC state exhibited both phenotypes (having both high and low NC ratios), our findings indicate an overall lower NC ratio in the population of cells in the PACC state compared to untreated cancer cells. In the future, it will be worthwhile to investigate this novel hybrid phenotype to reveal its relevance to cancer recurrence.

Abnormal nuclear morphology has been regarded as a distinct phenotype of malignant cancer cells that facilitates invasion, migration, and metastasis (54, 58, 61, 63). Nuclear circularity is a representative 2D feature that allows for the evaluation of morphological abnormalities and it is used as a diagnostic parameter by pathologists (56, 58, 127, 128). Sphericity is a 3D version of circularity that may provide better specificity due to the additional dimensional information (58, 129, 130). Treated cells exhibited an increasing nuclear volume and decreasing sphericity as a function of recovery time. Since the deformability of nuclei is closely related to the invasion ability during the

metastasis process (54, 68, 131), cells in the PACC state may exhibit a highly invasive morphological phenotype that facilitates cancer metastasis.

The life cycle of the PACC state has not yet been explored (31). One characteristic of cells in the PACC state is dormancy (28, 29, 31, 33, 35). Cells in the PACC state do not engage in the proliferative cell cycle, thereby avoiding cell cycle arrest at mitotic checkpoints due to genotoxic stress. This study, however, highlights that this dormancy phenotype is highly active, with evidence of repeated endocycling. Consequently, the presence of additional genomic material inside an enlarged nucleus may reinforce the genetic stability of these cells and enhance their resiliency against varied environmental stressors. It has been shown that a subset of cells in the PACC state eventually undergo some form of depolyploidization to generate resistant progeny and seed recurrence (31, 50, 132, 133). It is possible that the extra genomic material of cells in the PACC state might also enhance the ability to give rise to variable offspring and increase the likelihood of generating a resistant clone (134). Growing evidence into the role of the PACC states relevant to cancer lethality suggests that the PACC state is a “hallmark of lethal cancer” (31); nonetheless, the exact mechanisms of entry into the PACC state, the physiological changes during the dormant state, and the timing of and mechanisms utilized by cells in the PACC state to rapidly differentiate into therapeutic resistant cells remain unknown.

Ultimately, the findings presented in this study suggest that mononucleated cells in the PACC state are critical players in of the development of resistance to therapies and to eventual cancer recurrence (**Fig. 1**). Further characterization of the cellular and molecular programs that cancer cells in this newly-defined state can be leveraged to understand resistance phenotypes that contribute to cancer lethality.

Materials and Methods

Cell culture

PC3 and MDA-MB-231 cell lines were originally purchased from ATCC (United States). Cells were maintained in RPMI-1640 with L-Glutamine (for PC3 cells; Gibco, #11875-093) or DMEM (for MDA-MB-231 cells; Gibco, #11995-065), with 10% fetal bovine serum (FBS; Avantar, #97068-085) and 1% penicillin streptomycin (Gibco, #15140-122). Cells were cultured in standard conditions: 37°C, 5% CO_2 and were routinely checked for mycoplasma via LabCorp’s RT-qPCR mycoplasma contamination detection service.

Treatment

Sub-confluent cultures of PC3 cells were treated with [LD50] concentrations of cisplatin (6 μM; Millipore Sigma, #232120-50MG), docetaxel (5 nM; Cell Signaling Technology, #9886), or etoposide (25 μM; Cell Signaling Technology, #2200S) and cultured for 72 hours under standard conditions. MDA-MB-231 cells were treated with cisplatin at an [LD50] of 12 μM. Large cells were then sterilely isolated via size-restricted filtration with a pluriStrainer® 15 μm cell strainer (pluriSelect, #45-50015-03) and replated for culturing.

Nuclear morphological analysis

Large cells were generated as described, isolated, and then cultured for 1, 5, 10, and 15 days following 72 hours of drug treatment. 24 hours prior to each timepoint, the cells were seeded into 35 mm IbiTreat μ-Dishes (Ibidi USA Inc., #81156) and incubated overnight. Samples were fixed in 10% formalin for 20 minutes, and permeabilized for 10 minutes in 0.2% Triton-X-100 in PBS. Permeabilized samples were blocked with 10% goat serum in PBS at room temperature for 30 minutes. Samples were then incubated overnight at 4°C with a lamin A/C primary antibody (Table S1) and secondary antibody (Table S1) for 1 hour at room temperature. Samples were mounted with ProLong™ Diamond Antifade Mountant with DAPI (Invitrogen, #P36971) and images were acquired using a Zeiss Observer Z1 microscope/ZEN pro 2.0 software (Carl Zeiss Microscopy).

Nuclear morphology (mono-nucleated vs. multi-nucleated) was manually discriminated and counted using Fiji (135).

Nucleolar morphological analysis
Cells were induced, seeded, fixed, permeabilized, and blocked as described above. The samples were incubated with nucleolin and lamin A/C primary antibodies (Table S1) overnight at 4°C and a secondary antibody (Table S1) for 1 hour at room temperature, protected from light. Samples were mounted and images were acquired as described above. Images were analyzed for nucleolar number and area via a custom CellProfiler 4.0 (136) pipeline.

DNA damage response marker foci analysis
Treated cells were induced, seeded, fixed, permeabilized, and blocked as described above. Samples were incubated overnight at 4°C with gamma H2A.X, 53BP1, and lamin A/C primary antibodies (Table S1), followed by washes with 0.1% PBS-T. Appropriate secondary antibodies (Table S1) were incubated for 1 hour at room temperature, followed by five washes with 0.1% PBS-T. Antibodies were diluted with 1% (v/v) bovine serum albumin (BSA, Millipore Sigma, A9418) in PBS. Samples were mounted using ProLong™ Diamond Antifade Mountant with DAPI. Image acquisition was performed using a Zeiss Observer Z1 microscope/ZEN pro 2.0 software (Carl Zeiss Microscopy). Images were analyzed via a custom CellProfiler 4.0 pipeline.

Three-dimensional (3D), confocal, live-cell imaging
Live cells were incubated for 45 minutes at standard conditions with 1 µg/mL of CellTracker™ Orange CMTMR (Invitrogen, #C2927) and 10 µM Vybrant™ DyeCycle™ Green Stain (Molecular Probes, # V35004) to label the cytoplasm and nucleus, respectively. Labeled cells were lifted and resuspended in cold Matrigel Basement Matrix (Corning, #356232), plated onto 35 mm Ibidi μ-Dishes (glass bottom, Ibidi USA Inc., #81158), and immediately coverslipped. Plated samples were cultured for 30 minutes at standard conditions to allow for solidification of the Matrigel, and then covered with phenol-free RPMI-1640 with L-Glutamine (Gibco, #1835030) with 10% FBS and 1% penicillin streptomycin. Image acquisition was performed using a Nikon Eclipse Ti2 microscope with a Nikon C2 camera and NIS Elements version 5.11. (Nikon Inc.) with a live-cell imaging ThermoBox incubation system (Tokai Hit Co.). 3D image processing and analysis was performed with Imaris 9.8 software (Oxford Instruments).

Time-lapse imaging of PC3-FUCCI
PC3-FUCCI cells were plated and cultured overnight under standard conditions (see above) and then treated with 6 µM [LD50] cisplatin for 72 hours. After treatment, media was changed to fresh RPMI (see above) and live-cell timelapse microscopy of treated cells was performed in an Incucyte SX5 (Sartorius). Images were taken every 30 minutes in the phase, green, and orange channels.

Flow cytometry analysis
Live cells were incubated with an Autophagy Assay Kit (Red) (Abcam, #ab270790) according to the manufacturer's recommendation to label autophagosomes and FITC-Annexin V (BioLegend, #640906) according to the manufacturer's protocol to label apoptotic cells. Cells were analyzed on an Attune NxT Flow Cytometer (Thermo Fisher Scientific). At least 40,000 events were recorded per sample and acquired data was analyzed using FlowJo software version 10.8 (BD Biosciences).

Immunofluorescent imaging of autophagosomes
Cells were seeded into 35 mm IbiTreat μ-Dishes and cultured overnight. The cells were fixed and permeabilized as described above. Following permeabilization, samples were blocked with 10% BSA for 30 minutes. The samples were then incubated overnight at 4°C with LC3 A/B, lamin A/C, gamma H2A.X primary antibodies (Table S1) and subsequently washed with 0.1% (v/v) PBS-T. Samples were incubated for 1 hour at room temperature with appropriate secondary antibodies (Table S1), followed by washes with PBS-T. Samples were mounted with ProLong™ Diamond

Antifade Mountant with DAPI (see above). Images were acquired using a Zeiss Observer Z1 microscope and ZEN pro 2.0 software (Carl Zeiss Microscopy).

Autophagosome detection by 3D live-cell imaging

Live cells were labeled with 2 μM Calcein AM (Invitrogen, #C3100MP) for cytoplasm and Autophagy Assay Kit (Red) (Abcam, #ab270790) for 30 minutes under standard culture conditions as recommended by the manufacturer. Labeled cells were washed with HBSS, and phenol red-free media was added to culture dishes prior to imaging. Image acquisition was performed using a Nikon Eclipse Ti2 microscope with a Nikon C2 camera and NIS Elements version 5.11. (Nikon Inc.) with a live-cell imaging ThermoBox incubation system (Tokai Hit Co.). Image processing and analysis was performed with Imaris 9.8 software (Oxford Instruments).

Statistical analysis

All statistical analyses were performed in GraphPad Prism version 9.1 (GraphPad Software, LLC). An $\alpha = 0.05$ (confidence level 95%) was the criterion considered to determine statistical significance for all tests. No significance (ns), *, **, ***, and **** represent p values of ≥ 0.05, <0.05, <0.01, <0.001, and <0.0001, respectively. For violin plots, red lines indicate median and blue lines indicate lower and upper quartiles.

Acknowledgments

Kim, C-J was supported by the Basic Science Research Program through the National Research Foundation of Korea funded by the Ministry of Education (2021R1A6A3A14043146). Cho, Y-K was supported by Institute for Basic Science (IBS-R020-D1). Pienta, KJ was supported by National Cancer Institute grants U54CA143803, CA163124, CA093900, and CA143055, and the Prostate Cancer Foundation. Amend, SR was supported by the US Department of Defense CDMRP/PCRP (W81XWH-20-10353 and W81XWH-22-1-0680), the Patrick C. Walsh Prostate Cancer Research Fund, and the Prostate Cancer Foundation. The authors thank members of the Cancer Ecology Center for thoughtful discussion and feedback.

References

1. R. A. Burrell, C. Swanton, Tumour heterogeneity and the evolution of polyclonal drug resistance. *Mol Oncol* **8**, 1095-1111 (2014).
2. N. Mansoori *et al.*, Mycobacterium tuberculosis Complex Drug Resistance in a High Tuberculosis Incidence Area from the WHO Eastern Mediterranean Region. *J Pharm Pharm Sci* **20**, 428-434 (2017).
3. S. N. Aleksakhina, A. Kashyap, E. N. Imyanitov, Mechanisms of acquired tumor drug resistance. *Biochim Biophys Acta Rev Cancer* **1872**, 188310 (2019).
4. M. M. Gottesman, T. Fojo, S. E. Bates, Multidrug resistance in cancer: role of ATP-dependent transporters. *Nature reviews. Cancer* **2**, 48-58 (2002).
5. T. Shibue, R. A. Weinberg, EMT, CSCs, and drug resistance: the mechanistic link and clinical implications. *Nat Rev Clin Oncol* **14**, 611-629 (2017).
6. R. N. Ganapathi, M. K. Ganapathi, Mechanisms regulating resistance to inhibitors of topoisomerase II. *Frontiers in pharmacology* **4**, 89 (2013).
7. R. H. Chisholm, T. Lorenzi, J. Clairambault, Cell population heterogeneity and evolution towards drug resistance in cancer: Biological and mathematical assessment, theoretical treatment optimisation. *Biochim Biophys Acta* **1860**, 2627-2645 (2016).
8. M. Nikolaou, A. Pavlopoulou, A. G. Georgakilas, E. Kyrodimos, The challenge of drug resistance in cancer treatment: a current overview. *Clin Exp Metastasis* **35**, 309-318 (2018).
9. I. A. Cree, P. Charlton, Molecular chess? Hallmarks of anti-cancer drug resistance. *BMC cancer* **17**, 10 (2017).
10. K. J. Pienta, A. W. Partin, D. S. Coffey, Cancer as a disease of DNA organization and dynamic cell structure. *Cancer research* **49**, 2525-2532 (1989).

11. F. Du, H. Liu, Y. Lu, X. Zhao, D. Fan, Epithelial-to-Mesenchymal Transition: Liaison between Cancer Metastasis and Drug Resistance. *Crit Rev Oncog* **22**, 275-282 (2017).
12. I. Dagogo-Jack, A. T. Shaw, Tumour heterogeneity and resistance to cancer therapies. *Nat Rev Clin Oncol* **15**, 81-94 (2018).
13. N. McGranahan, C. Swanton, Clonal Heterogeneity and Tumor Evolution: Past, Present, and the Future. *Cell* **168**, 613-628 (2017).
14. C. E. Meacham, S. J. Morrison, Tumour heterogeneity and cancer cell plasticity. *Nature* **501**, 328-337 (2013).
15. A. Marusyk, K. Polyak, Tumor heterogeneity: causes and consequences. *Biochim Biophys Acta* **1805**, 105-117 (2010).
16. N. Andor *et al.*, Pan-cancer analysis of the extent and consequences of intratumor heterogeneity. *Nat Med* **22**, 105-113 (2016).
17. S. Turajlic, A. Sottoriva, T. Graham, C. Swanton, Resolving genetic heterogeneity in cancer. *Nat Rev Genet* **20**, 404-416 (2019).
18. D. R. Caswell, C. Swanton, The role of tumour heterogeneity and clonal cooperativity in metastasis, immune evasion and clinical outcome. *BMC Med* **15**, 133 (2017).
19. M. Greaves, C. C. Maley, Clonal evolution in cancer. *Nature* **481**, 306-313 (2012).
20. R. J. Gillies, D. Verduzco, R. A. Gatenby, Evolutionary dynamics of carcinogenesis and why targeted therapy does not work. *Nature reviews. Cancer* **12**, 487-493 (2012).
21. R. Gatenby, J. Brown, The Evolution and Ecology of Resistance in Cancer Therapy. *Cold Spring Harb Perspect Med* **8** (2018).
22. D. Hanahan, R. A. Weinberg, The hallmarks of cancer. *Cell* **100**, 57-70 (2000).
23. M. D. Kuczler, A. M. Olseen, K. J. Pienta, S. R. Amend, ROS-induced cell cycle arrest as a mechanism of resistance in polyaneuploid cancer cells (PACCs). *Prog Biophys Mol Biol* **165**, 3-7 (2021).
24. M. D. Kuczler, A. M. Olseen, K. J. Pienta, S. R. Amend, ROS-induced cell cycle arrest as a mechanism of resistance in polyaneuploid cancer cells (PACCs). *Progress in Biophysics and Molecular Biology* **165**, 3-7 (2021).
25. D. T. Fox, D. E. Soltis, P. S. Soltis, T.-L. Ashman, Y. Van De Peer, Polyploidy: A Biological Force From Cells to Ecosystems. *Trends in Cell Biology* **30**, 688-694 (2020).
26. S. R. Amend *et al.*, Polyploid giant cancer cells: Unrecognized actuators of tumorigenesis, metastasis, and resistance. *The Prostate* **79**, 1489-1497 (2019).
27. K. J. Pienta, E. U. Hammarlund, R. Axelrod, J. S. Brown, S. R. Amend, Poly-aneuploid cancer cells promote evolvability, generating lethal cancer. *Evolutionary Applications* **13**, 1626-1634 (2020).
28. L. G. Kostecka, K. J. Pienta, S. R. Amend, Lipid droplet evolution gives insight into polyaneuploid cancer cell lipid droplet functions. *Medical Oncology* **38** (2021).
29. K.-C. Lin *et al.*, An in vitro tumor swamp model of heterogeneous cellular and chemotherapeutic landscapes. *Lab on a Chip* **20**, 2453-2464 (2020).
30. L. G. Kostecka *et al.*, High KIFC1 expression is associated with poor prognosis in prostate cancer. *Medical Oncology* **38** (2021).
31. K. J. Pienta, E. U. Hammarlund, J. S. Brown, S. R. Amend, R. M. Axelrod, Cancer recurrence and lethality are enabled by enhanced survival and reversible cell cycle arrest of polyaneuploid cells. *Proceedings of the National Academy of Sciences* **118**, e2020838118 (2021).
32. K. J. Pienta *et al.*, Cancer cells employ an evolutionarily conserved polyploidization program to resist therapy. *Seminars in cancer biology* 10.1016/j.semcancer.2020.11.016 (2020).
33. M. M. Mallin, K. J. Pienta, S. R. Amend, Cancer cell foraging to explain bone-specific metastatic progression. *Bone* 10.1016/j.bone.2020.115788, 115788 (2020).
34. A. M. Alharbi, A. M. De Marzo, J. L. Hicks, T. L. Lotan, J. I. Epstein, Prostatic Adenocarcinoma With Focal Pleomorphic Giant Cell Features A Series of 30 Cases. *Am J Surg Pathol* **42**, 1286-1296 (2018).

35. R. Mirzayans, B. Andrais, D. Murray, Roles of Polyploid/Multinucleated Giant Cancer Cells in Metastasis and Disease Relapse Following Anticancer Treatment. *Cancers* **10**, 118 (2018).
36. T. Illidge, Polyploid giant cells provide a survival mechanism for p53 mutant cells after DNA damage. *Cell Biology International* **24**, 621-633 (2000).
37. J. Chen *et al.*, Polyploid Giant Cancer Cells (PGCCs): The Evil Roots of Cancer. *Current Cancer Drug Targets* **19**, 360-367 (2019).
38. S. K. Martin *et al.*, Multinucleation and Mesenchymal-to-Epithelial Transition Alleviate Resistance to Combined Cabazitaxel and Antiandrogen Therapy in Advanced Prostate Cancer. *Cancer Research* **76**, 912-926 (2016).
39. W. H. Wolberg, W. Nick Street, O. L. Mangasarian, Importance of Nuclear Morphology in Breast Cancer Prognosis. *Clinical Cancer Research* **5**, 3542-3548 (1999).
40. J. Liu, The dualistic origin of human tumors. *Seminars in Cancer Biology* **53**, 1-16 (2018).
41. R. Virchow *et al.*, *Cellular pathology as based upon physiological and pathological histology; twenty lectures delivered in the Pathological Institute of Berlin during the months of February, March, and April, 1858* (John Churchill, London, 1860).
42. K.-C. Lin *et al.*, The role of heterogeneous environment and docetaxel gradient in the emergence of polyploid, mesenchymal and resistant prostate cancer cells. *Clinical & Experimental Metastasis* **36**, 97-108 (2019).
43. T. L. Orr-Weaver, When bigger is better: the role of polyploidy in organogenesis. *Trends in Genetics* **31**, 307-315 (2015).
44. S. K. Pandit, B. Westendorp, A. de Bruin, Physiological significance of polyploidization in mammalian cells. *Trends in Cell Biology* **23**, 556-566 (2013).
45. Y. Van De Peer, S. Maere, A. Meyer, The evolutionary significance of ancient genome duplications. *Nature Reviews Genetics* **10**, 725-732 (2009).
46. H. O. Lee, J. M. Davidson, R. J. Duronio, Endoreplication: polyploidy with purpose. *Genes & Development* **23**, 2461-2477 (2009).
47. L. Comai, The advantages and disadvantages of being polyploid. *Nature Reviews Genetics* **6**, 836-846 (2005).
48. W. Derks, O. Bergmann, Polyploidy in Cardiomyocytes. *Circulation Research* **126**, 552-565 (2020).
49. S. M. A. Lens, R. H. Medema, Cytokinesis defects and cancer. *Nature Reviews Cancer* **19**, 32-45 (2019).
50. I. Vitale *et al.*, Illicit survival of cancer cells during polyploidization and depolyploidization. *Cell Death & Differentiation* **18**, 1403-1413 (2011).
51. G. Gentric, C. Desdouets, Polyploidization in Liver Tissue. *The American Journal of Pathology* **184**, 322-331 (2014).
52. K. J. Gjelsvik, R. Besen-McNally, V. P. Losick, Solving the Polyploid Mystery in Health and Disease. *Trends in Genetics* **35**, 6-14 (2019).
53. M. Webster, K. L. Witkin, O. Cohen-Fix, Sizing up the nucleus: nuclear shape, size and nuclear-envelope assembly. *Journal of Cell Science* **122**, 1477-1486 (2009).
54. C. Denais, J. Lammerding, "Nuclear Mechanics in Cancer". (Springer New York, 2014), 10.1007/978-1-4899-8032-8_20, pp. 435-470.
55. N. Kumar *et al.*, Computer-extracted features of nuclear morphology in hematoxylin and eosin images distinguish colon tumors. *The Journal of Pathology* **257**, 17-28 (2022).
56. D. Sengupta *et al.*, A deep hybrid learning pipeline for accurate diagnosis of ovarian cancer based on nuclear morphology. *PLOS ONE* **17**, e0261181 (2022).
57. K. Damodaran, M. Crestani, D. S. Jokhun, G. V. Shivashankar, Nuclear morphometrics and chromatin condensation patterns as disease biomarkers using a mobile microscope. *PLOS ONE* **14**, e0218757 (2019).
58. A. F. J. Janssen, S. Y. Breusegem, D. Larrieu, Current Methods and Pipelines for Image-Based Quantitation of Nuclear Shape and Nuclear Envelope Abnormalities. *Cells* **11**, 347 (2022).

59. H. Mi *et al.*, Predictive models of response to neoadjuvant chemotherapy in muscle-invasive bladder cancer using nuclear morphology and tissue architecture. *Cell Reports Medicine* **2**, 100382 (2021).
60. L. Hou *et al.*, Dataset of segmented nuclei in hematoxylin and eosin stained histopathology images of ten cancer types. *Scientific Data* **7** (2020).
61. L. F. Flores *et al.*, Nuclear Dynamics and Chromatin Structure: Implications for Pancreatic Cancer. *Cells* **10**, 2624 (2021).
62. C. Uhler, G. V. Shivashankar, Nuclear Mechanopathology and Cancer Diagnosis. *Trends in Cancer* **4**, 320-331 (2018).
63. E. G. Fischer, Nuclear Morphology and the Biology of Cancer Cells. *Acta Cytologica* **64**, 511-519 (2020).
64. B. M. Skinner, E. E. P. Johnson, Nuclear morphologies: their diversity and functional relevance. *Chromosoma* **126**, 195-212 (2017).
65. C. Koch *et al.*, Characterization of circulating breast cancer cells with tumorigenic and metastatic capacity. *EMBO Molecular Medicine* **12** (2020).
66. A. C. Zambon *et al.*, Methods and sensors for functional genomic studies of cell-cycle transitions in single cells. *Physiol Genomics* **52**, 468-477 (2020).
67. F. Alisafaei, D. S. Jokhun, G. V. Shivashankar, V. B. Shenoy, Regulation of nuclear architecture, mechanics, and nucleocytoplasmic shuttling of epigenetic factors by cell geometric constraints. *Proceedings of the National Academy of Sciences* **116**, 13200-13209 (2019).
68. T. Fischer, A. Hayn, C. T. Mierke, Effect of Nuclear Stiffness on Cell Mechanics and Migration of Human Breast Cancer Cells. *Frontiers in Cell and Developmental Biology* **8** (2020).
69. G. R. Kidiyoor *et al.*, ATR is essential for preservation of cell mechanics and nuclear integrity during interstitial migration. *Nature Communications* **11** (2020).
70. T. Takaki *et al.*, Actomyosin drives cancer cell nuclear dysmorphia and threatens genome stability. *Nature Communications* **8**, 16013 (2017).
71. D. Hernandez-Verdun, Assembly and disassembly of the nucleolus during the cell cycle. *Nucleus* **2**, 189-194 (2011).
72. C. M. Caragine, S. C. Haley, A. Zidovska, Nucleolar dynamics and interactions with nucleoplasm in living cells. *eLife* **8** (2019).
73. D. L. J. Lafontaine, J. A. Riback, R. Bascetin, C. P. Brangwynne, The nucleolus as a multiphase liquid condensate. *Nature Reviews Molecular Cell Biology* **22**, 165-182 (2021).
74. L. Latonen, Phase-to-Phase With Nucleoli – Stress Responses, Protein Aggregation and Novel Roles of RNA. *Frontiers in Cellular Neuroscience* **13** (2019).
75. M. C. Lafita-Navarro, M. Conacci-Sorrell, Nucleolar stress: From development to cancer. *Semin Cell Dev Biol* 10.1016/j.semcdb.2022.04.001 (2022).
76. K. Yang, J. Yang, J. Yi, Nucleolar stress: Hallmarks, sensing mechanism and diseases. *Cell Stress* **2**, 125-140 (2018).
77. I. Orsolic *et al.*, The relationship between the nucleolus and cancer: Current evidence and emerging paradigms. *Seminars in Cancer Biology* **37-38**, 36-50 (2016).
78. J. Diesch, R. D. Hannan, E. Sanij, Perturbations at the ribosomal genes loci are at the centre of cellular dysfunction and human disease. *Cell & Bioscience* **4**, 43 (2014).
79. S. E. Polo, S. P. Jackson, Dynamics of DNA damage response proteins at DNA breaks: a focus on protein modifications. *Genes & Development* **25**, 409-433 (2011).
80. P. G. Pilié, C. Tang, G. B. Mills, T. A. Yap, State-of-the-art strategies for targeting the DNA damage response in cancer. *Nature Reviews Clinical Oncology* **16**, 81-104 (2019).
81. H. D. Popp, S. Brendel, W.-K. Hofmann, A. Fabarius, Immunofluorescence Microscopy of H2AX and 53BP1 for Analyzing the Formation and Repair of DNA Double-strand Breaks. *Journal of Visualized Experiments* 10.3791/56617 (2017).
82. E. Bártová, S. Legartová, M. Dundr, J. Suchánková, A role of the 53BP1 protein in genome protection: structural and functional characteristics of 53BP1-dependent DNA repair. *Aging* **11**, 2488-2511 (2019).

83. E. Moeglin *et al.*, Uniform Widespread Nuclear Phosphorylation of Histone H2AX Is an Indicator of Lethal DNA Replication Stress. *Cancers* **11**, 355 (2019).
84. K. Rothkamm *et al.*, DNA damage foci: Meaning and significance. *Environmental and Molecular Mutagenesis* **56**, 491-504 (2015).
85. L. R. van Veelen *et al.*, Analysis of ionizing radiation-induced foci of DNA damage repair proteins. *Mutation Research/Fundamental and Molecular Mechanisms of Mutagenesis* **574**, 22-33 (2005).
86. B. Meyer *et al.*, Clustered DNA damage induces pan-nuclear H2AX phosphorylation mediated by ATM and DNA–PK. *Nucleic Acids Research* **41**, 6109-6118 (2013).
87. D. Ding *et al.*, Induction and inhibition of the pan-nuclear gamma-H2AX response in resting human peripheral blood lymphocytes after X-ray irradiation. *Cell Death Discovery* **2**, 16011 (2016).
88. S. d. Feraudy, I. Revet, V. Bezrookove, L. Feeney, J. E. Cleaver, A minority of foci or pan-nuclear apoptotic staining of γH2AX in the S phase after UV damage contain DNA double-strand breaks. *Proceedings of the National Academy of Sciences* **107**, 6870-6875 (2010).
89. R. Mathew, V. Karantza-Wadsworth, E. White, Role of autophagy in cancer. *Nature Reviews Cancer* **7**, 961-967 (2007).
90. L. Koepke *et al.*, An improved method for high-throughput quantification of autophagy in mammalian cells. *Scientific Reports* **10** (2020).
91. G. Kroemer *et al.*, Classification of cell death: recommendations of the Nomenclature Committee on Cell Death 2009. *Cell Death & Differentiation* **16**, 3-11 (2009).
92. M. Yao *et al.*, Autophagy-Mediated Clearance of Free Genomic DNA in the Cytoplasm Protects the Growth and Survival of Cancer Cells. *Frontiers in Oncology* **11** (2021).
93. L. Vera-Ramirez, S. K. Vodnala, R. Nini, K. W. Hunter, J. E. Green, Autophagy promotes the survival of dormant breast cancer cells and metastatic tumour recurrence. *Nature Communications* **9** (2018).
94. S. G. Mathiassen, D. De Zio, F. Cecconi, Autophagy and the Cell Cycle: A Complex Landscape. *Frontiers in Oncology* **7** (2017).
95. G. Kroemer, B. Levine, Autophagic cell death: the story of a misnomer. *Nat Rev Mol Cell Biol* **9**, 1004-1010 (2008).
96. A. G. Eliopoulos, S. Havaki, V. G. Gorgoulis, DNA Damage Response and Autophagy: A Meaningful Partnership. *Frontiers in Genetics* **7** (2016).
97. M.-E. Papandreou, N. Tavernarakis, Nucleophagy: from homeostasis to disease. *Cell Death & Differentiation* **26**, 630-639 (2019).
98. P. Jevtić, L. J. Edens, L. D. Vuković, D. L. Levy, Sizing and shaping the nucleus: mechanisms and significance. *Current Opinion in Cell Biology* **28**, 16-27 (2014).
99. R. Kumar *et al.*, Supraphysiologic Testosterone Induces Ferroptosis and Activates Immune Pathways through Nucleophagy in Prostate Cancer. *Cancer Research* **81**, 5948-5962 (2021).
100. D. Zhang, Y. Wang, S. Zhang, Asymmetric Cell Division in Polyploid Giant Cancer Cells and Low Eukaryotic Cells. *BioMed Research International* **2014**, 1-8 (2014).
101. K. J. Pienta *et al.*, Cancer cells employ an evolutionarily conserved polyploidization program to resist therapy. *Seminars in Cancer Biology* 10.1016/j.semcancer.2020.11.016 (2020).
102. J. Erenpreisa, A. Huna, K. Salmina, T. R. Jackson, M. S. Cragg, Macroautophagy-aided elimination of chromatin. *Autophagy* **8**, 1877-1881 (2012).
103. R. Rajaraman, M. Rajaraman, S. Rajaraman, D. Guernsey, Neosis – a paradigm of self-renewal in cancer. *Cell Biology International* **29**, 1084-1097 (2005).
104. J. Chen *et al.*, Polyploid Giant Cancer Cells (PGCCs): The Evil Roots of Cancer. *Current cancer drug targets* **19**, 360-367 (2019).
105. P.-E. Puig *et al.*, Tumor cells can escape DNA-damaging cisplatin through DNA endoreduplication and reversible polyploidy. *Cell Biology International* **32**, 1031-1043 (2008).

106. E. Mukhtar, V. M. Adhami, H. Mukhtar, Targeting Microtubules by Natural Agents for Cancer Therapy. *Molecular Cancer Therapeutics* **13**, 275-284 (2014).
107. J. Erenpreisa *et al.*, Polyploid tumour cells elicit paradiploid progeny through depolyploidizing divisions and regulated autophagic degradation. *Cell Biol Int* **35**, 687-695 (2011).
108. S. White-Gilbertson, C. Voelkel-Johnson, Giants and monsters: Unexpected characters in the story of cancer recurrence. *Adv Cancer Res* **148**, 201-232 (2020).
109. D. Zhang, Y. Wang, S. Zhang, Asymmetric cell division in polyploid giant cancer cells and low eukaryotic cells. *Biomed Res Int* **2014**, 432652 (2014).
110. Z. Zhang *et al.*, Irradiation-induced polyploid giant cancer cells are involved in tumor cell repopulation via neosis. *Mol Oncol* 10.1002/1878-0261.12913 (2021).
111. K. Mittal *et al.*, Multinucleated polyploidy drives resistance to Docetaxel chemotherapy in prostate cancer. *British journal of cancer* **116**, 1186-1194 (2017).
112. M. Sundaram, D. L. Guernsey, M. M. Rajaraman, R. Rajaraman, Neosis: a novel type of cell division in cancer. *Cancer Biol Ther* **3**, 207-218 (2004).
113. S. Gupta, R. Santoro, Regulation and Roles of the Nucleolus in Embryonic Stem Cells: From Ribosome Biogenesis to Genome Organization. *Stem Cell Reports* **15**, 1206-1219 (2020).
114. J. E. FitzGerald, M. Grenon, N. F. Lowndes, 53BP1: function and mechanisms of focal recruitment. *Biochem Soc Trans* **37**, 897-904 (2009).
115. A. Gupta *et al.*, Role of 53BP1 in the regulation of DNA double-strand break repair pathway choice. *Radiat Res* **181**, 1-8 (2014).
116. M. Mirza-Aghazadeh-Attari *et al.*, 53BP1: A key player of DNA damage response with critical functions in cancer. *DNA Repair (Amst)* **73**, 110-119 (2019).
117. L. B. Schultz, N. H. Chehab, A. Malikzay, T. D. Halazonetis, P53 Binding Protein 1 (53bp1) Is an Early Participant in the Cellular Response to DNA Double-Strand Breaks. *Journal of Cell Biology* **151**, 1381-1390 (2000).
118. S. Panier, S. J. Boulton, Double-strand break repair: 53BP1 comes into focus. *Nature Reviews Molecular Cell Biology* **15**, 7-18 (2014).
119. M. Zimmermann, T. De Lange, 53BP1: pro choice in DNA repair. *Trends in Cell Biology* **24**, 108-117 (2014).
120. A. Gupta *et al.*, Role of 53BP1 in the Regulation of DNA Double-Strand Break Repair Pathway Choice. *Radiation Research* **181**, 1-8 (2014).
121. M. Löbrich, P. Jeggo, A Process of Resection-Dependent Nonhomologous End Joining Involving the Goddess Artemis. *Trends in Biochemical Sciences* **42**, 690-701 (2017).
122. K. Karanam, A. Loewer, G. Lahav, Dynamics of the DNA damage response: insights from live-cell imaging. *Briefings in Functional Genomics* **12**, 109-117 (2013).
123. X. Yue, C. Bai, D. Xie, T. Ma, P.-K. Zhou, DNA-PKcs: A Multi-Faceted Player in DNA Damage Response. *Frontiers in Genetics* **11** (2020).
124. M. Krajewska, R. Fehrmann, E. de Vries, M. van Vugt, Regulators of Homologous Recombination Repair as Novel Targets for Cancer Treatment. *Frontiers in Genetics* **6** (2015).
125. V. Nandakumar *et al.*, Isotropic 3D Nuclear Morphometry of Normal, Fibrocystic and Malignant Breast Epithelial Cells Reveals New Structural Alterations. **7**, e29230 (2012).
126. G. E. Neurohr *et al.*, Excessive Cell Growth Causes Cytoplasm Dilution And Contributes to Senescence. *Cell* **176**, 1083-1097.e1018 (2019).
127. H. Huang *et al.*, Cancer diagnosis by nuclear morphometry using spatial information. *Pattern Recognition Letters* **42**, 115-121 (2014).
128. M. Schöchlin *et al.*, A nuclear circularity-based classifier for diagnostic distinction of desmoplastic from spindle cell melanoma in digitized histological images. *J Pathol Inform* **5**, 40-40 (2014).
129. A. N. Coyne, J. D. Rothstein, Nuclear lamina invaginations are not a pathological feature of C9orf72 ALS/FTD. *Acta Neuropathologica Communications* **9** (2021).
130. R. Goswami *et al.*, Mechanical Shielding in Plant Nuclei. *Current Biology* **30**, 2013-2025.e2013 (2020).

131. E. S. Bell, J. Lammerding, Causes and consequences of nuclear envelope alterations in tumour progression. *European Journal of Cell Biology* **95**, 449-464 (2016).
132. K. R. Verena Rohnalter, Florian Finkernagel, Till Adhikary, Julia Obert, Kristina Dorzweiler, Maike Bensberg, Sabine Muller-Brusselbach, Rolf Muller, A multi-stage process including transient polyploidization and EMT precedes the emergence of chemoresistent ovarian carcinoma cells with a dedifferentiated and pro-inflammatory secretory phenotype. *Oncotarget* **6**, 21 (2015).
133. K. C. Lin *et al.*, Epithelial and mesenchymal prostate cancer cell population dynamics on a complex drug landscape. *Convergent science physical oncology* **3** (2017).
134. J. Heng, H. H. Heng, Two-phased evolution: Genome chaos-mediated information creation and maintenance. *Prog Biophys Mol Biol* **165**, 29-42 (2021).
135. J. Schindelin *et al.*, Fiji: an open-source platform for biological-image analysis. *Nat Methods* **9**, 676-682 (2012).
136. D. R. Stirling *et al.*, CellProfiler 4: improvements in speed, utility and usability. *BMC Bioinformatics* **22**, 433 (2021).

Figures

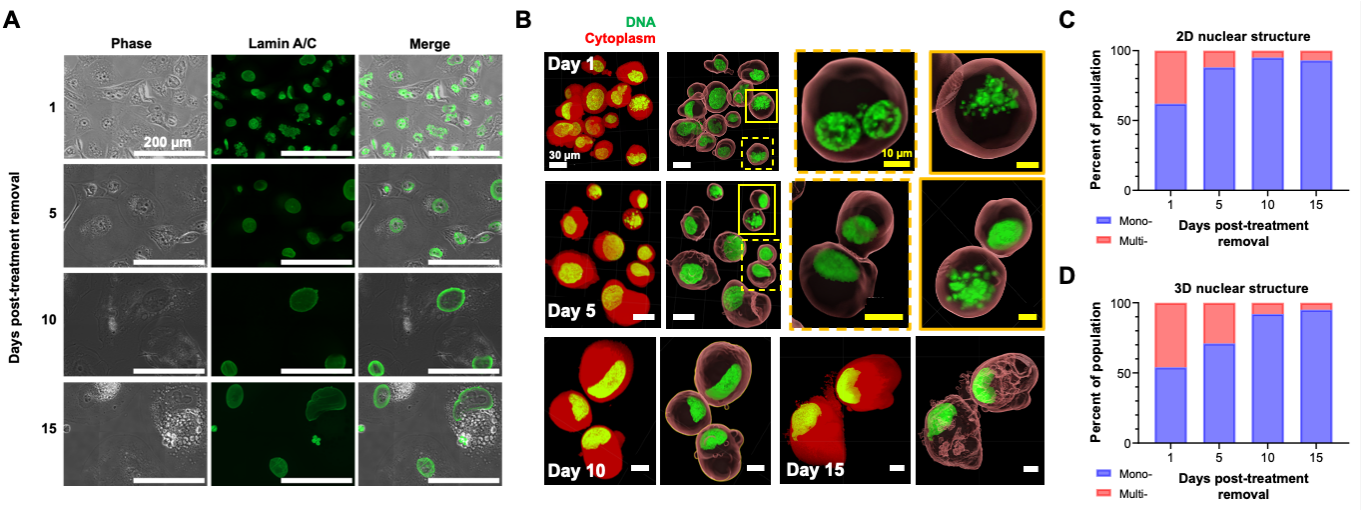

Figure 1. Characterization of the nuclear morphology of cisplatin-treated prostate cancer cells. Representative immunofluorescence images **(A)** to demonstrate the nuclear morphology of treated PC3 cells generated with 72h [LD50] cisplatin treatment following removal from chemotherapy. **(B)** Live treated PC3 cells at various timepoints in recovery were suspended in Matrigel and staining DNA with Vybrant™ DyeCycle™ Green Stain (for DNA) and CellTracker™ Orange (for cytoplasm). 3D images were obtained via confocal microscopy and images were rendered and volumes determined using Imaris 9.8 software. **(C)** Population distribution of mononucleated and multinucleated PC3s, derived from images described in (A). Nuclear morphology (mononucleated vs. multinucleated) was manually discriminated and counted using Fiji. At least 250 cells were analyzed per condition. **(D)** Nuclear morphology was also determined using the 3D imaging described in (B).

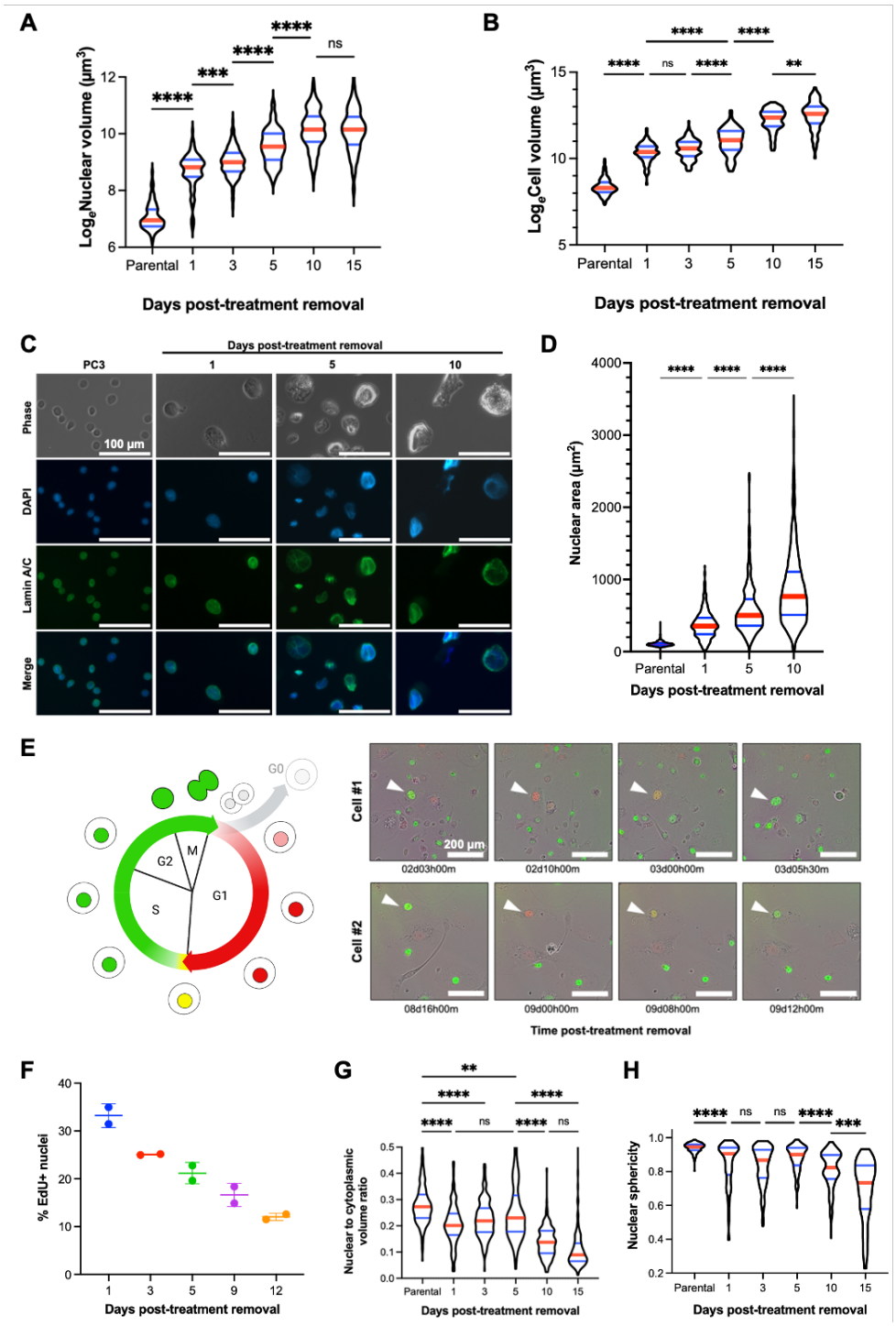

Figure 2. Characterization of treated cancer cell nuclear size. Natural log-transformed **(A)** nuclear volume and **(B)** cellular volume of live treated PC3 cells, generated with 72h [LD50] cisplatin treatment, at various timepoints in recovery was determined by suspending cells in Matrigel and staining DNA with Vybrant™ DyeCycle™ Green Stain (for DNA) and CellTracker™ Orange (for cytoplasm). 3D images were obtained via confocal microscopy and images were rendered for volumetric determination using Imaris 9.8 software. Data was analyzed for differences

between groups using a one-way ANOVA, a post-hoc Tukey's multiple comparisons tests was used to detect between-group differences. **(C)** Nuclei were isolated from parental and treated PC3 cells before mounting on PLL-coated dishes. Nuclei were stained for lamin A/C and covered with ProLong™ Diamond Antifade Mountant with DAPI before imaging on a Zeiss Observer Z1 microscope. The size of isolated nuclei was quantitated **(D)** via a custom CellProfiler 4.0 pipeline. A Kruskal-Wallis test was used to analyze if there were any significant differences among the samples, Dunn's multiple comparison's test used to test for comparisons between groups. To look for evidence of endocycling, PC3 cells were transduced with a FUCCI reporter, treated PC3s were generated from this reporter cell line, and timelapse microscopy **(E)** was performed with an Incucyte SX5 with images taken every 30min. Two representative cells are shown. **(F)** Cisplatin-treated PC3s were tested for *de novo* DNA synthesis via a Click-It Plus EdU assay according to the manufacturer's protocol. Images were acquired using the 10x objective on a Zeiss Observer Z1 microscope. A custom CellProfiler pipeline was developed and used to quantify DAPI+Edu+ nuclei. **(G)** Nuclear and cytoplasmic volumes were used to calculate a nuclear to cytoplasmic volume ratio of treated PC3s at various timepoints past treatment removal. A Kruskal-Wallis test was used to analyze if there were any significant differences among the samples, Dunn's multiple comparison's test used to test for comparisons between groups. From the 3D nuclear rendering in Imaris, nuclear sphericity **(H)** was determined. A Kruskal-Wallis test was used to analyze if there were any significant differences among the samples, with a Dunn's multiple comparison's post-hoc test. For all statistical tests: * = $p<0.05$, ** = $p<0.01$, *** = $p<0.001$, **** = $p<0.0001$.

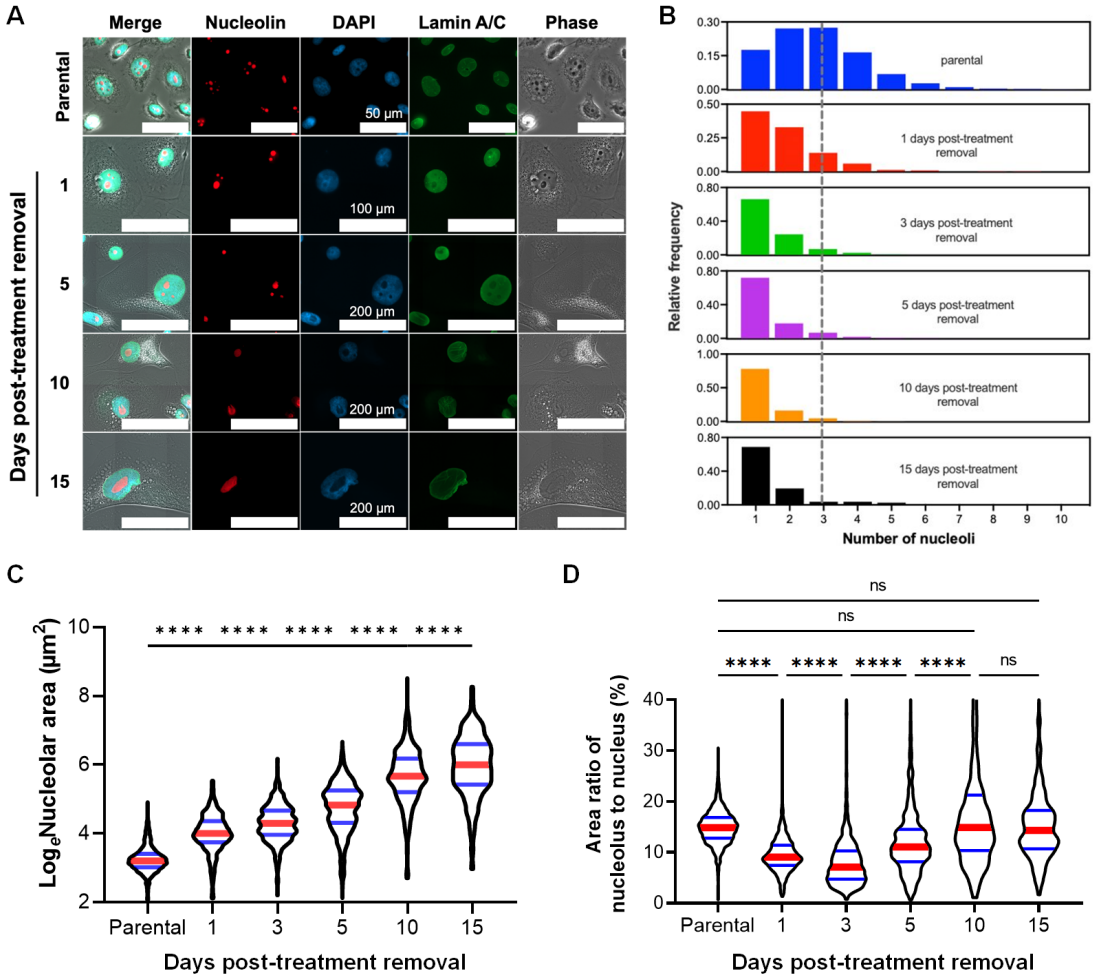

Figure 3. Nucleolar counts, size, and molecular signatures. Treated PC3 cancer cells generated with 72h [LD50] cisplatin treatment were stained for lamin A/C and nucleolin, and were mounted with DAPI, **(A)** representative images of nucleoli are shown. A custom CellProfiler 4.0 pipeline was used to then determine the **(B)** number and **(C)** area of the nucleoli of the treated PC3s throughout the recovery period to become PACCs. Nucleolar area was analyzed for differences between groups using a one-way ANOVA, and a post-hoc Tukey's multiple comparisons test was used to detect between-group differences. The lamin A/C stain was used to calculate nuclear area, and thus **(D)** the nucleolar to nuclear area ratio at each timepoint post-treatment removal could be calculated; a Kruskal-Wallis test was used to analyze if there were any significant differences among the samples, with a Dunn's multiple comparison's post-hoc test. For all statistical tests: * = p<0.05, ** = p<0.01, *** = p<0.001, **** = p<0.0001.

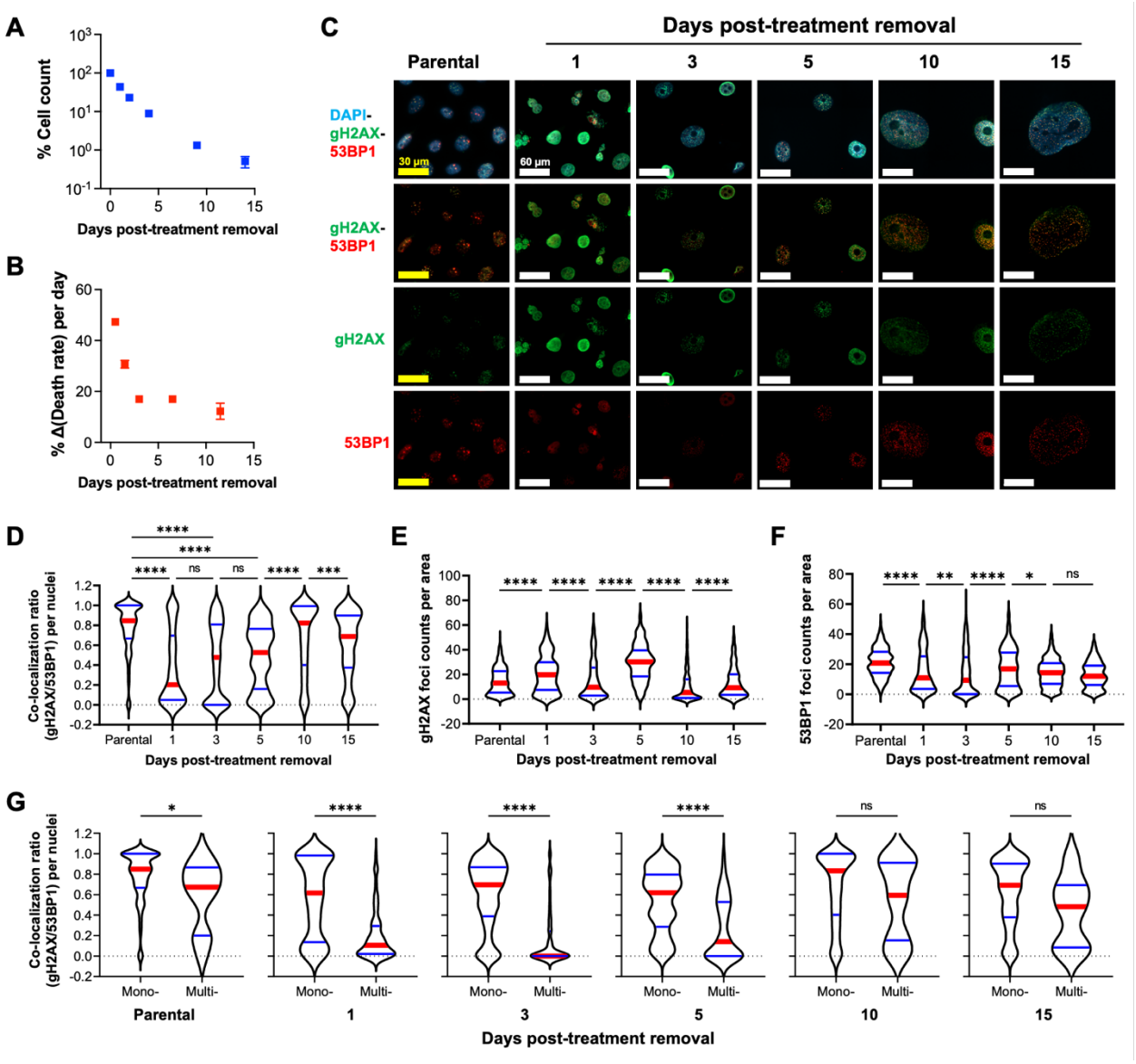

Figure 4. The DNA damage response in cisplatin-treated prostate cancer cells. Relative cell number (percent normalized to population count at 0 days post-treatment removal) as a function of recovery time **(A)** was determined for treated PC3 cells generated with 72h [LD50] cisplatin treatment. From this data, we also determined **(B)** the percent change in the death rate for each of the recovery days we investigated. **(C)** Immunofluorescence staining and imaging was used to visualize genomic contents (DAPI), sites of DNA damage (gH2AX), and DDR machinery recruitment (53BP1). From these images, a custom CellProfiler 4.0 pipeline was used to determine **(D)** the colocalization ratio of gH2AX with 53BP1, as well as a raw count per unit cellular area of the number of **(E)** gH2AX foci and **(F)** 53BP1 foci. For each day post-treatment recovery, were classified as mononucleates and multinucleates, and **(G)** the colocalization ratio of gH2AX with 53BP1 was determined for each cell class. Mann-Whitney tests were used to detect differences between groups in (D) through (G). For all statistical tests: * = $p<0.05$, ** = $p<0.01$, *** = $p<0.001$, **** = $p<0.0001$.

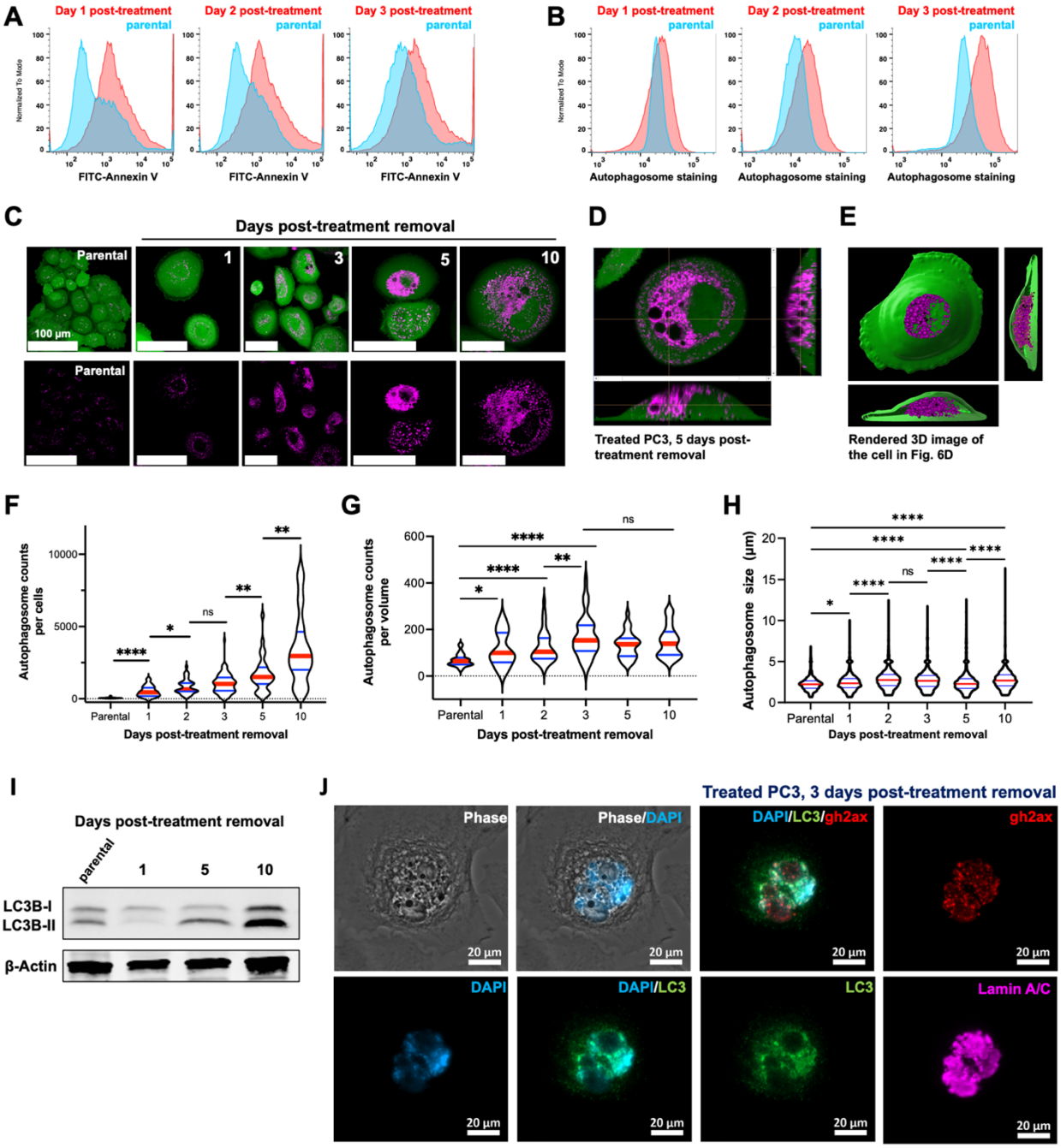

Figure 5. Treated prostate cancer cell death: apoptosis and autophagy. Flow cytometry was used to measure **(A)** surface expression of annexin V as a marker of apoptosis and **(B)** staining of autophagosomes (via Abcam's Autophagy Assay kit) in treated PC3s generated with 72h [LD50] cisplatin treatment at days 1, 2, and 3 post-treatment removal compared to parental PC3 prostate cancer cells. The cytoplasm of live treated PC3s was labeled with Calcein AM, and the Autophagy Assay kit was similarly used to fluorescently label autophagosomes/autolysosomes for **(C)** 2D and **(D)** 3D imaging (pink = autophagic vesicles, green = cytoplasm). Additionally, **(E)** 3D images were rendered using Imaris 9.8 and **(F)** per cell autophagic vesicle counts were determined. **(G)** these counts were also normalized to cellular volume. Mann-Whitney tests were used to detect differences between groups in (F) and (G). **(H)** Imaris was also used to measure the diameter of individual autophagosomes at the different recovery days investigated in this experiment,

differences between groups were detected using a one-way ANOVA, and a post-hoc Tukey's multiple comparisons test was used to detect between-group differences. Western blotting **(I)** was used to examine the expression of the autophagy-related proteins LC3B-I and LC3B-II over treated PC3 recovery. **(J)** Immunofluorescent microscopy was also used to examine treated PC3 for colocalization of DAPI, gH2AX, and LC3 as evidence of nucleophagy. For all statistical tests: * = $p<0.05$, ** = $p<0.01$, *** = $p<0.001$, **** = $p<0.0001$.

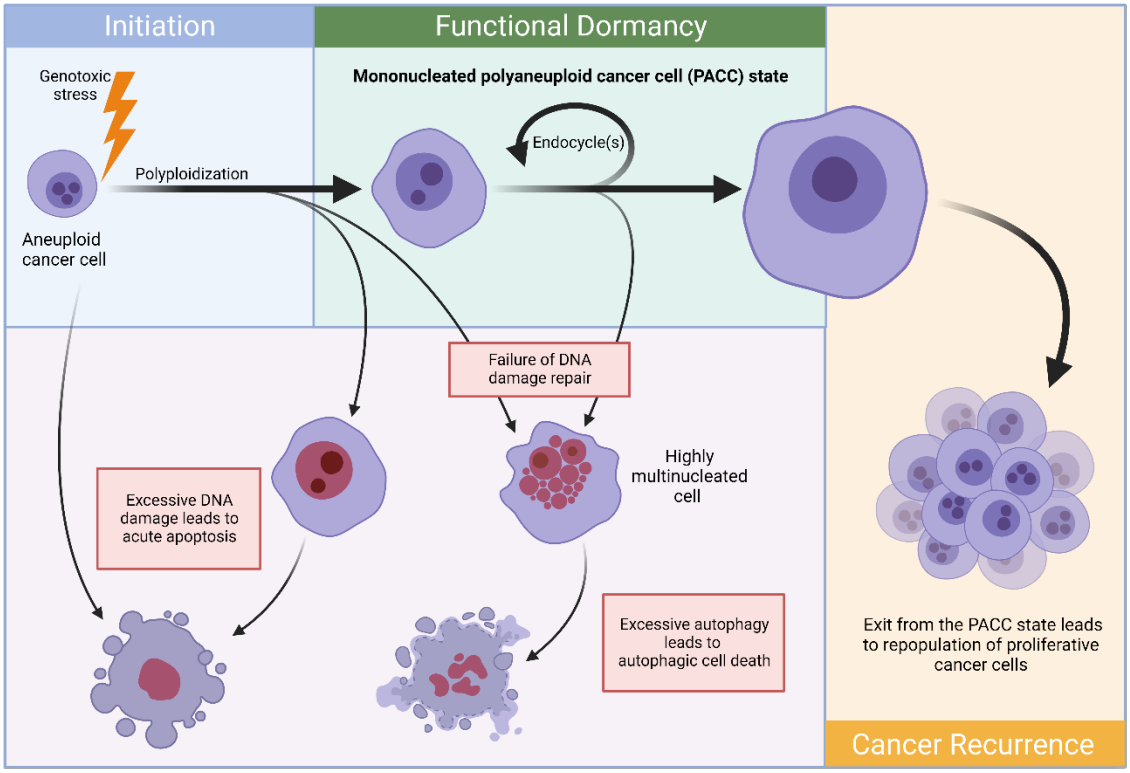

Figure 6. Schematic illustration of the proposed polyaneuploid cancer cell (PACC) life cycle. Initially, an aneuploid cancer cell experiences a temporary genotoxic stress. This can result in multiple trajectories: excessive DNA damage can occur before polyploidization, causing apoptosis; the cancer cell can undergo whole-genome duplication to become polyaneuploid, but then still have accumulated a burden of DNA damage high enough to lead to acute apoptosis; similarly, this polyaneuploid cell can attempt to repair its damaged genome but ultimately fail, becoming highly multinucleated and dying; lastly, it can undergo whole-genome duplication and become a viable mononucleated *polyaneuploid cancer cell (PACC)*. This PACC begins its period of functional dormancy, characterized by increases in cellular and nuclear volume that can be attributed to one or more endocycles. Not all PACCs survive until the end of this functional dormancy period: a sub-population will further try to repair DNA damage and also will experience heightened levels of autophagy as they try to achieve cellular homeostasis, ultimately leading to autophagic cell death. Eventually, after a period of time removed from the stressor, the recovered PACC state is reached. This PACC is capable of eventual depolyploidization that results in the revival of the aneuploid cancer cell population.

Supporting Information

Supplementary Text

Materials and Methods

Nuclei isolation

Cells were lifted, washed twice with PBS, and stored on ice. Nuclei extraction buffer (NEB) was prepared on ice and consisted of final concentrations of 10 mM HEPES (Life Technologies Corp., #15630-080), 1.5 mM $MgCl_2$, 10 mM KCl, 0.25% NP-40 (Thermo Scientific, #95124), and 1X protease/phosphatase inhibitor (Thermo Scientific, #1861281) diluted in ultrapure deionized water. 500 μL of NEB was added per $1x10^6$ cells, samples were mixed six times via pipetting and then placed on ice for 10 minutes. Samples were pelleted for 10 seconds in a compact benchtop centrifuge, and the supernatants containing cytoplasmic components were removed. This was repeated twice more, with 5-minute incubations on ice. Following the final removal of supernatants, samples were resuspended in 10% formalin, fixed for 10 minutes, and then filtered through a 70 μm cell strainer. The fixed/filtered nuclei were then pelleted with a quick spin, formalin was removed, and nuclei were resuspended in PBS. Nuclei suspensions were allowed to adhere to 35 mm Ibidi μ-Dishes (glass bottom, Ibidi USA Inc., #81158) pre-coated with Poly-L-Lysine (EMD Millipore Corp., #A-005-C) for 30 minutes at room temperature. Once any non-adhered nuclei were washed away, samples were permeabilized with 0.5% Triton-X 100 in PBS and stained for immunofluorescence imaging, then covered with ProLong™ Diamond Antifade Mountant with DAPI. Images were analyzed for nuclear area via a custom CellProfiler 4.0 pipeline.

Western blotting

Cells were lysed in ice-cold lysis buffer [150 mmol/L NaCl, 1% Triton X-100, 0.5% sodium deoxycholate, 0.1% SDS, 50 mmol/L Tri (pH 8.0), protease inhibitor cocktail (Roche)], and cell debris was removed by centrifugation at 4 °C for 10 minutes at 12,000 rpm. Equal masses of protein were resolved via SDS-PAGE (gels: Bio-Rad Laboratories, #4561095) and transferred onto Trans-Blot Turbo nitrocellulose membranes (Bio-Rad Laboratories, #1704158). Membranes were blocked with 1X casein blocking buffer (Sigma–Aldrich, #B6429,) for 1 hour at room temperature, then incubated with primary antibodies against LC3B, β-Actin and appropriate secondary antibodies (see Table S1). Blots were imaged on a LICOR Odyssey and quantified by ImageJ software. The relative protein expression level in each sample was normalized to the internal control.

FUCCI cell line generation

$1.5x10^6$ HEK-293T cells were plated in 10 cm dishes in DMEM supplemented with 10% FBS. After 24 hours, cells were transfected for second generation lentivirus packaging as follows: 1 μg of Ki67p-T2A-FUCCI plasmid(67) (gifted from Alexander Zambon) and 1 μg of psPAX2:pMD2.g (packaging:envelope) at an 8:1 ratio were diluted in 200 μL of OptiMEM media (Gibco, #31985062). Both psPAX2 (Addgene plasmid #12260; http://n2t.net/addgene:12260 ; RRID:Addgene_12260) and pMD2.g (Addgene plasmid #12259; http://n2t.net/addgene:12259 ; RRID:Addgene_12259) were a gift from Didier Trono. 5 μL of X-tremeGENE HP transfection reagent (Roche, #XTGHP-RO) was added, and the solution was mixed by pipetting and incubated for 30 minutes before being added dropwise onto the HEK-293Ts. After 18-20 hours, media was changed to the target cell media plus 30% heat inactivated FBS. Packaging cells were allowed to condition media for 48 hours before viral harvest. Viral media was removed and filtered through a Millex HP 0.45 μm PES syringe filter (Millipore, #SLHPM33RS). Lentivirus from 1-2 10 cm dishes (10-20 mL) was concentrated using Clontech Lenti-X concentrator (Takara, #631232) per the manufacturer's protocol. The viral pellet was resuspended in target cell media supplemented with 30% heat inactivated FBS and added onto PC3 cells ($3.5x10^5$/well) in 6-well plate along with 10 μg/mL Polybrene Infection Reagent (Millipore, #TR-1003). PC3 cells were transduced for 20 hours before media was changed to fresh supplemented RPMI. After 3 days of

recovery, cells were selected with 5 µg/mL blasticidin (Gibco, #A1113903) and expression of reporters was assessed on an EVOS FL Auto imaging system (Life Technologies) with GFP (for mAG) and TxRed (for mCherry) light cubes. Clones were generated from the selected cell pool via limiting dilution cloning.

EdU incorporation assay

Large cells were generated as described and then cultured for 1, 3, 5, 9, and 12 days after being filtered following 72 hours of drug treatment. The cells then were seeded on 12 mm round coverslips in 24-well plates. Once cells adhered, the media was replaced and supplemented with 10 µM EdU (Molecular Probes, #E10187). After a 20-hour incubation period under standard conditions, the Click-It Plus EdU assay (Molecular Probes, #C10640) was performed according to the manufacturer's protocol. Coverslips were mounted to slides using ProLong™ Diamond Antifade Mountant with DAPI (see above). Images were acquired using the 10x objective on the Zeiss Observer Z1 microscope and ZEN pro 2.0 software (Carl Zeiss Microscopy). A custom CellProfiler pipeline was developed and used to quantify total number of nuclei in the tiled image based on DAPI signal and number of EdU-positive nuclei based on AlexaFluor™ 647 signal within nuclei boundaries.

Ribosomal RNA gel electrophoresis

Total RNA was isolated from cells using the PureLink™ RNA Mini Kit (Invitrogen, # 12183025). A mass of 100 ng total RNA was prepared for gel electrophoresis and run on a 1% agarose-TBE gel with ethidium bromide. Gels were imaged on a Bio-Rad ChemiDoc™ XRS+ and 28s, 18s, and 5.8s ribosomal RNA bands could be observed.

Supplementary Figures

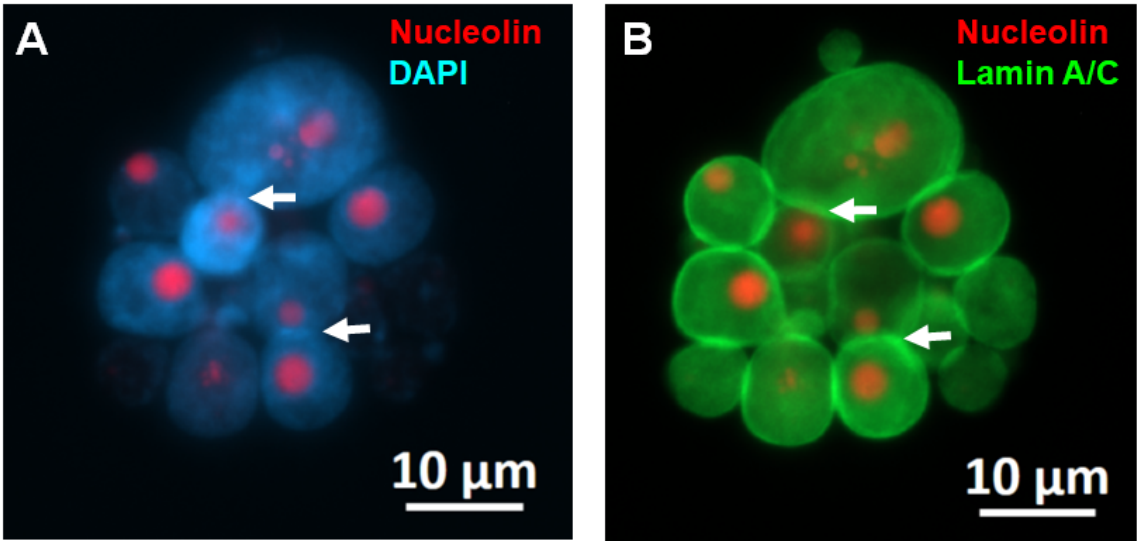

Figure S1. Differences in nuclear visualization between DAPI and lamin A/C. A cisplatin-treated PC3 cancer cell 1 day post-treatment removal was stained for nucleolin and lamin A/C and mounted with DAPI prior to immunofluorescent imaging. Differences in the ability of **(A)** DAPI vs. **(B)** lamin A/C to discriminate individual nuclei should be noted.

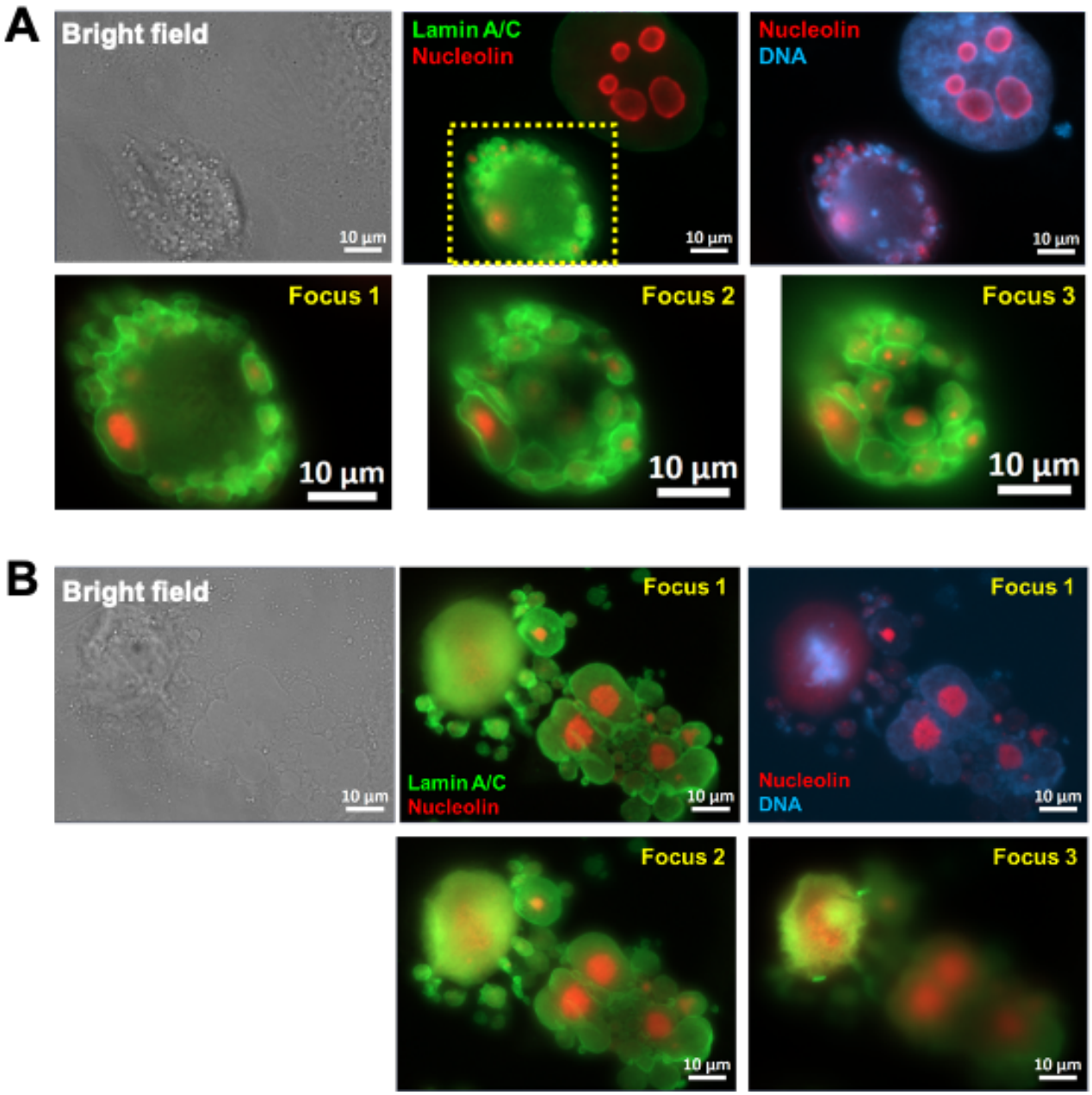

Figure S2. Effects of focal plane on morphologic discrimination of multinucleated cells. Treated PC3s induced with 72h [LD50] cisplatin treatment were stained for lamin A/C, nucleolin, and mounted with DAPI. **(A)** and **(B)** show two different examples of cells where the number of micronuclei/extent of multinucleation might be missed in 2D immunofluorescent microscopy due the effect of different focal planes and cell height.

Figure S3. Ki67p-T2A-FUCCI construct. Gifted from Alexander Zambon.

Sphericity	X-Y view	Additional angled view
0.932		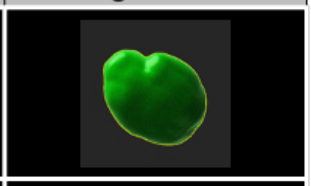
0.826	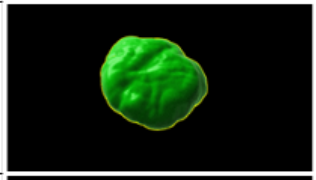	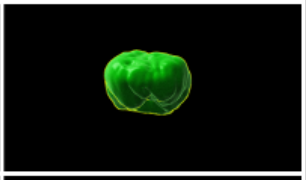
0.740	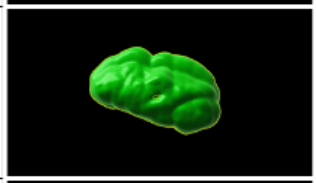	
0.618		
0.515	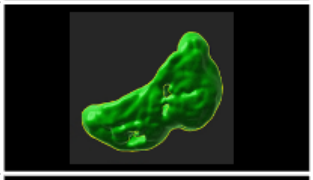	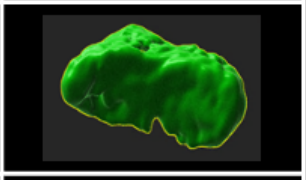
0.431	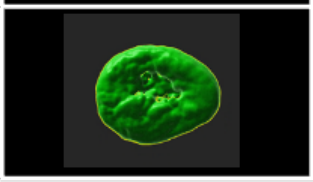	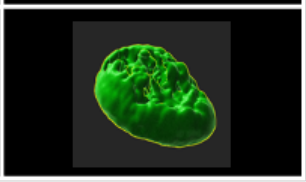

Figure S4. Visual reference for differences in sphericity. Live recovered cells 15 days post-treatment removal were stained with 10 μM Vybrant™ DyeCycle™ Green Stain. 3D confocal images were acquired and nuclear shapes were rendered in Imaris 9.8 prior to sphericity calculations.

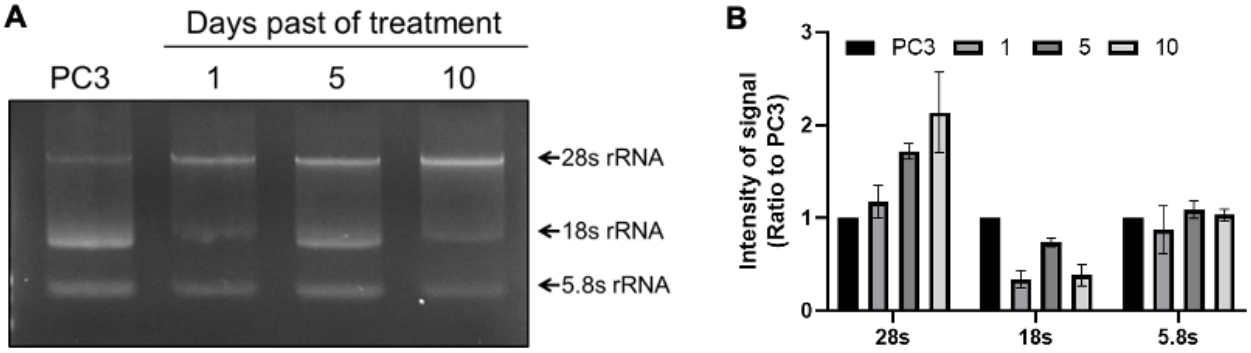

Figure S5. Ribosomal RNA expression levels in treated PC3s. RNA was isolated from treated PC3s induced with 72h [LD50] cisplatin at various points following treatment removal. **(A)** 100 ng total RNA was resolved via gel electrophoresis, and the rRNA pattern (28s, 18s and 5.8s rRNA) signals was observed via staining with EtBr. **(B)** Densitometry was used to quantitate differences in rRNA levels from three independent replicates.

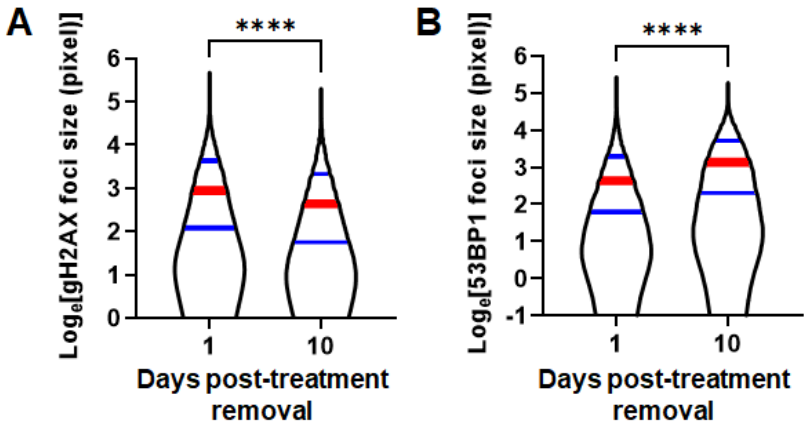

Figure S6. gh2ax and 53bp1 foci size in cisplatin treated PC3s 1 and 10 post-treatment removal. Treated PC3s were generated with 72h [LD50] cisplatin treatment and immunofluorescence staining/imaging was used to visualize genomic contents (DAPI), sites of DNA damage (gH2AX), and DDR machinery recruitment (53BP1). A custom CellProfiler 4.0 pipeline was used to determine **(A)** the size of gH2AX foci and **(B)** the size of 53BP1 foci. Mann-Whitney tests were used to detect differences between groups, **** = $p<0.0001$.

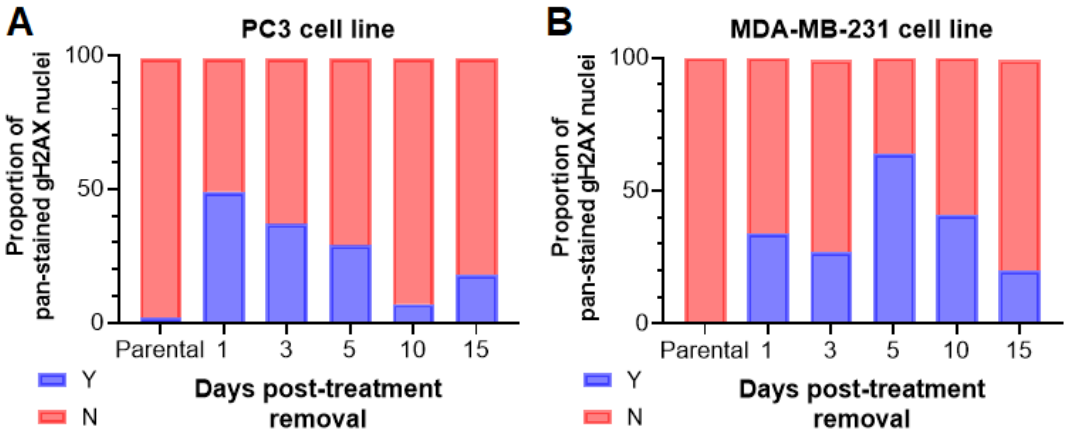

Figure S7. Pan-staining of gh2ax in cisplatin-treated PC3 prostate cancer cells vs. MDA-MB-231 breast cancer cells. Graphs show the relative proportion of cells with (Y) and without (N) gH2AX pan-stained nuclei from analyze immunofluorescent microscopy images in **(A)** treated PC3 cells and **(B)** treated MDA-MB-231 cells, both generated with 72h [LD50] cisplatin treatment.

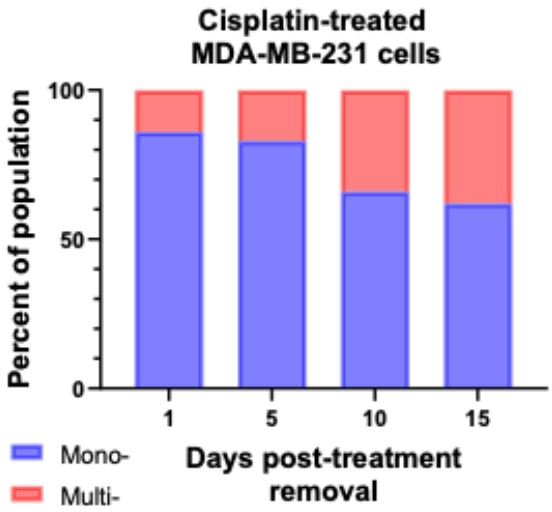

Figure S8. Characterization of treated MDA-MB-231 nuclear morphology. Population distribution of mononucleated and multinucleated treated MDA-MB-231s generated with 72h [LD50] cisplatin treatment, derived from immunofluorescent images of cells stained for lamin A/C and mounted with DAPI. Nuclear morphology (mononucleated vs. multinucleated) was manually discriminated and counted using Fiji software.

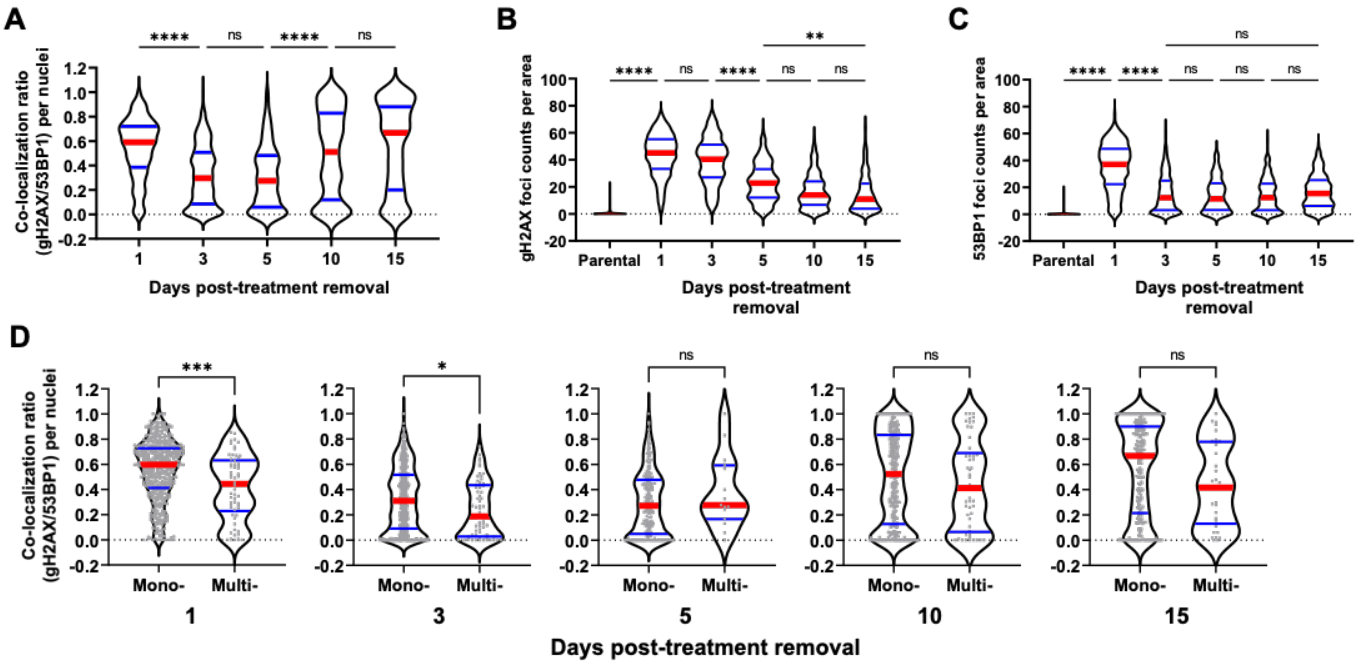

Figure S9. DDR foci analysis in treated MDA-MB-231 breast cancer cells. Treated MDA-MB-231s were generated with 72h [LD50] cisplatin treatment and immunofluorescence staining/imaging was used to visualize genomic contents (DAPI), sites of DNA damage (gH2AX), and DDR machinery recruitment (53BP1). Again, a custom CellProfiler 4.0 pipeline was used to determine **(A)** the colocalization ratio of gH2AX with 53BP1, as well as a raw count per unit cellular area of the number of **(B)** gH2AX foci and **(C)** 53BP1 foci. **(D)** For each day post-treatment recovery, were classified as mononucleates and multinucleates, and the colocalization ratio of gH2AX with 53BP1 was determined for each cell class. Mann-Whitney tests were used to detect differences between groups. For all statistical tests: * = $p<0.05$, ** = $p<0.01$, *** = $p<0.001$, **** = $p<0.0001$.

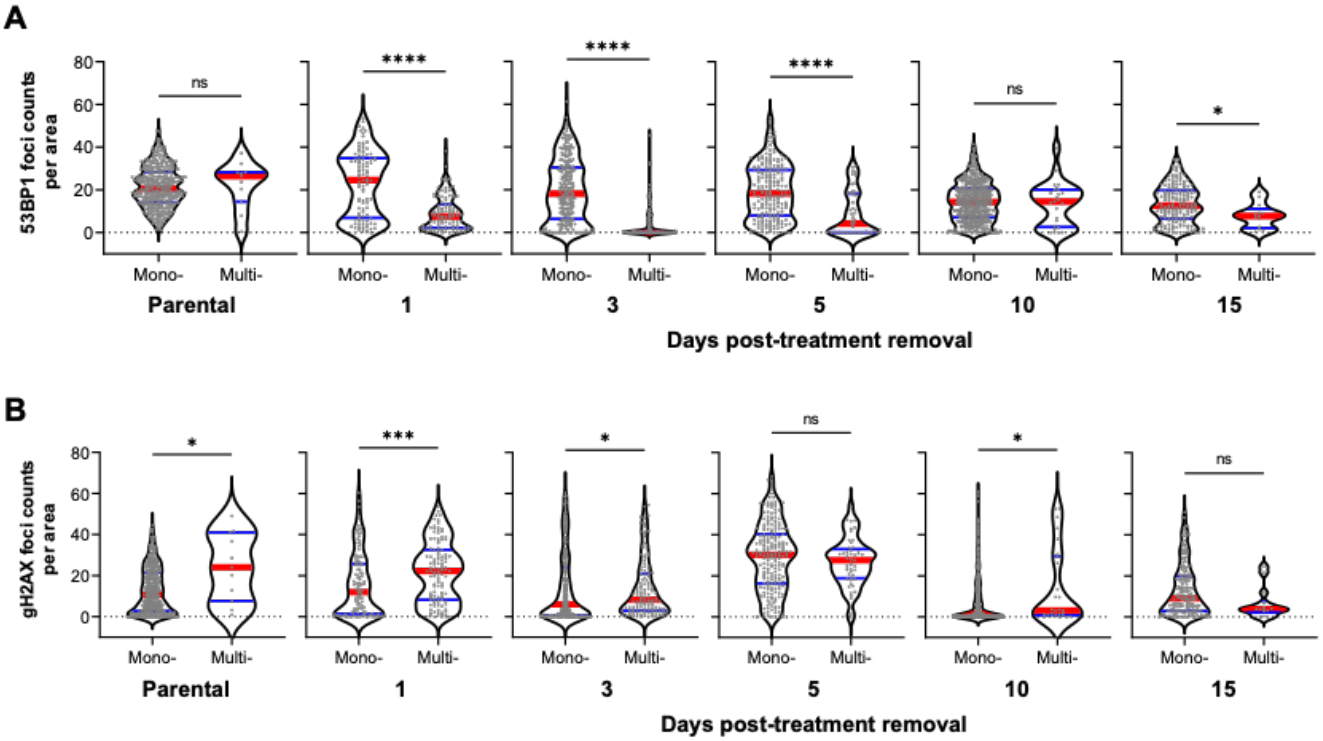

Figure S10. DDR foci counts in mononucleated vs. multinucleated treated MDA-MB-231s. Treated MDA-MB-231 cells were generated with 72h [LD50] cisplatin treatment and immunofluorescence staining/imaging was used to visualize genomic contents (DAPI), sites of DNA damage (gH2AX), and DDR machinery recruitment (53BP1). As a follow-up to Fig. S6, raw counts per unit cellular area of the number of **(A)** 53BP1 foci and **(B)** gH2AX foci were determined for mononucleate vs. multinucleate cells.

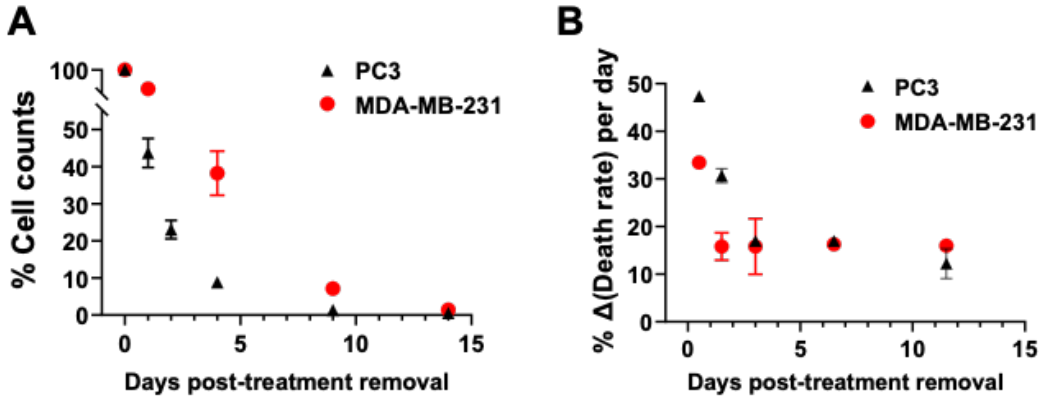

Figure S11. Differences in survival between treated PC3s and treated MDA-MB-231s. Relative cell number (percent normalized to population count at 0 days post-treatment removal) as a function of recovery time **(A)** was determined for treated MDA-MB-231s and treated PC3s generated with 72h [LD50] cisplatin treatment. From this data, we also determined **(B)** the percent change in the death rate for each of the recovery days we investigated.

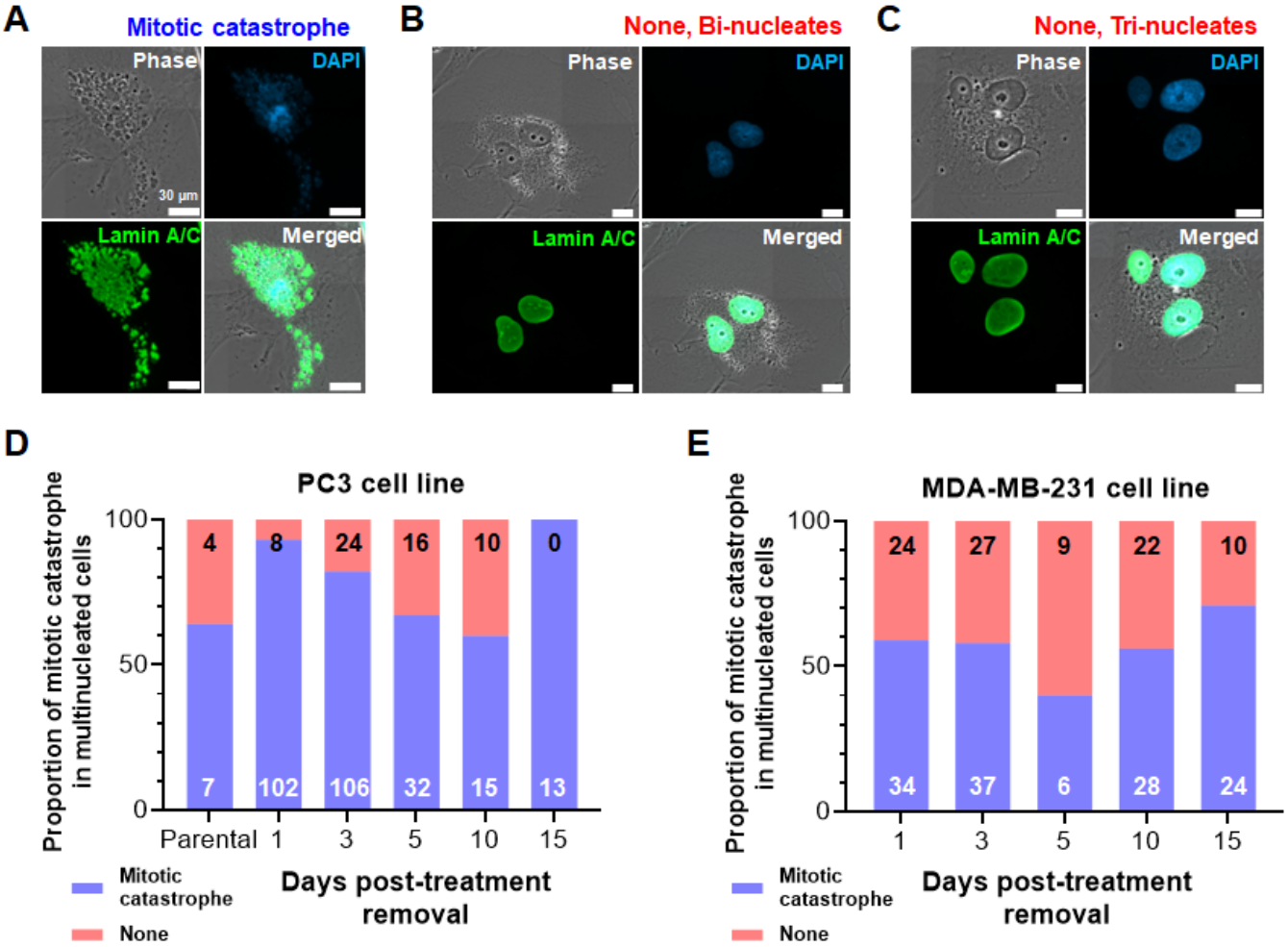

Figure S12. Proportion of mitotic catastrophe in multinucleated cisplatin-treated PC3s and MDA-MB-231s. Treated PC3s and **(A-C)** MDA-MB-231s were generated with 72h [LD50] cisplatin treatment and stained for lamin A/C and mounted with DAPI. Mononucleated, multinucleated, and mitotically catastrophic cells were classified via a custom CellProfiler 4.0 pipeline, and **(D-E)** the proportion of multinucleated cells to those experiencing mitotic catastrophe were plotted across the different days post-treatment removal for each cell line. The number of cells, which were observed in this experiment, were written on the bars (white: cells underwent mitotic catastrophe; black: cells were not underwent mitotic catastrophe). Multinucleated cells mostly consist of bi-nucleates, but few tri-nucleates with a certain number of cells underwent mitotic catastrophe.

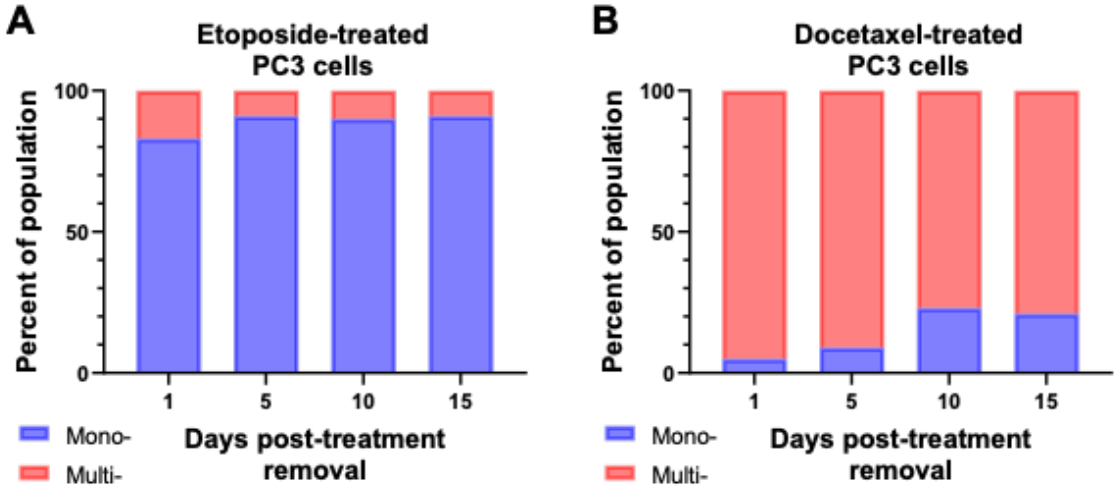

Figure S13. Nuclear morphology of treated PC3s generated with etoposide or docetaxel treatment. Population distribution of mononucleated and multinucleated treated PC3 cells generated with 72h **(A)** [LD50] etoposide treatment or **(B)** [LD50] docetaxel treatment, derived from immunofluorescent images of cells stained for lamin A/C and mounted with DAPI. Nuclear morphology (mononucleated vs. multinucleated) was discriminated and counted in Fiji software.

Supplementary Table S1. Antibodies used in this study

Primary antibodies

Antigen	Species	Dilution	Source
lamin A/C and	Mouse IgG2a	1:100 (IF)	Cell Signaling Technologies, #4777
Alexa FluorTM 647-conjugated nucleolin	Rabbit	1:50 (IF)	Abcam, #ab202709
gamma H2A.X	Mouse IgG1	1:250 (IF)	Abcam, #ab22551
53BP1	Rabbit	1:100 (IF)	Abcam, #ab175933
LC3A/B	Rabbit	1:100 (IF)	Cell Signaling Technology, #12741
LC3B	Rabbit	1:1000 (WB)	Cell signaling, #3868
β-Actin	Mouse	1:10000 (WB)	Millipore Sigma, #A5441

Secondary antibodies

Conjugate	Host species	IgG species	Dilution	Source
Alexa Fluor 488	goat	Mouse IgG1	1:1000 (IF)	Invitrogen, #A21121
Alexa Fluor 594	goat	Rabbit	1:1000 (IF)	Invitrogen, #A32740
Alexa Fluor 647	goat	Mouse IgG2a	1:500 (IF)	Invitrogen, #A21241
IRDye 680RD	goat	Mouse IgG	1:20,000 (WB)	LI-COR Biosciences, #926-68070
IRDye 800CW	goat	Rabbit	1:15,000 (WB)	LI-COR Biosciences, #926-32211